https://doi.org/10.1016/j.biomaterials.2020.120378

Photocrosslinkable nanocomposite ink for printing strong, biodegradable and bioactive bone graft

Yuhe Yang[a,b,1], Qiang Zhang[a,1], Tianpeng Xu[a], Hongyu Zhang[c], Ming Zhang[a], Li Lu[b], Yuefeng Hao[d,*], Jerry Y. H. Fuh[b,*,*], and Xin Zhao[a,*,*,*]

[a] Department of Biomedical Engineering, The Hong Kong Polytechnic University, Hung Hom, Kowloon, Hong Kong, China

[b] Department of Mechanical Engineering, National University of Singapore (NUS), 117575, Singapore

[c] State Key Laboratory of Tribology, Department of Mechanical Engineering, Tsinghua University, Beijing 100084, China

[d] Orthopedics and Sports Medicine Center, The Affiliated Suzhou Hospital of Nanjing Medical University, China

*Corresponding author: Orthopedics and Sports Medicine Center, The Affiliated Suzhou Hospital of Nanjing Medical University, Suzhou, Jiangsu 215000, China

**Corresponding author: Department of Mechanical Engineering, National University of Singapore (NUS), 117575, Singapore

***Corresponding author: Department of Biomedical Engineering, The Hong Kong Polytechnic University, Hung Hom, Kowloon, Hong Kong, China

E-mail address xin.zhao@polyu.edu.hk (X. Zhao); jerry.fuh@nus.edu.sg (J. Fuh); haoyuefeng@njmu.edu.cn (Y.F. Hao)

[1]These authors contributed equally to this work

Abstract

3D printing is known as a cost-effective technique that shows huge potential in fabrication of graft substitutes for bone tissue regeneration. However, the tradeoff between 3D printability, mechanical strength and bioactivity of the printed materials (i.e., inks) remains a challenge. In this work, we present a novel photocrosslinkable nanocomposite ink composed of tri-block poly (lactide-*co*-propylene glycol-*co*-lactide) dimethacrylate (P_mL_nDMA, m and n respectively represent the unit length of propylene glycol and lactide) and hydroxyethyl methacrylate (HEMA)-functionalized hydroxyapatite nanoparticles (nHAMA). The reactive HEMA-conjugated nHAMA, is designed to covalently crosslink with the surrounding polymer matrix to further increase the interfacial bonding between them. We find that the nHAMA can rapidly interact with P_mL_nDMA upon light exposure within 140 seconds and form an inorganic-organic co-crosslinked nanocomposite network, further enhancing the nanofiller-matrix interfacial compatibility. Notably, our nanocomposites possess significantly improved mechanical performances compared to the polymer, with compressive modulus increasing by nearly 10 times (from ~40 to ~400 MPa). Moreover, thanks to the low exothermic heat generation (< 37°C) during photocrosslinking, our nanocomposite ink enables facile encapsulation and long-term release of heat-labile biomolecules like bone morphogenic protein-2 (BMP-2). Furthermore, it demonstrates a readily tunable rheological property, wettability, degradation, and printability as a 3D bone scaffold. Together with its superior osteogenic ability both *in vitro* and *in vivo*, we envision that our nanocomposite ink holds great promise in 3D printing of bone grafts.

Key words: photocrosslinkable nanocomposite ink, 3D printing, mechanical reinforcement, bone regeneration

1. Introduction

Large-scale bone defect caused by injuries, diseases or trauma is one of the biggest challenges in orthopedic surgery since the damaged bone tissue lacks the ability of self-repairing and complete remodeling [1, 2]. Although autografts and allografts are clinically approved and exhibit satisfactory therapeutic efficacy, they are limited by donor site morbidity, immune and inflammatory responses, and risk of disease transmission [3]. To circumvent these issues, tissue engineering techniques has attracted extensive attention as an innovative alternative [4, 5]. In particular, 3D printing, shows great potential in the rapid and accurate fabrication of bone tissue engineering scaffolds according to the patients' needs. Due to its high reproducibility and resolution, 3D printing can construct bone scaffolds with well-controlled geometry to accommodate complex bone defects, as well as adequate 3D porous structures and interconnectivity to allow the exchange of oxygen and nutrients, metabolite elimination and host tissue ingrowth [6].

Among various 3D printing techniques, extrusion-based printing is most commonly adopted due to its relatively simple set-up, low operation cost, and high printing speed [7]. In a typical extrusion-based printing process, the inks will be extruded from a nozzle, deployed to the specific position, and then rapidly stabilized to maintain the fidelity of the structure. Frequently used inks like polymers including polycaprolactone (PCL) and poly(lacticco-glycolic acid) (PLGA) have showed good printability and mechanical strength in bone scaffold fabrication. However, to make these materials printable, organic solvents or heat-up process have to be involved, sacrificing their capability to encapsulate bioactive molecules [8, 9]. Photocrosslinkable monomers such as hydroxyethyl methacrylate (HEMA), methylmethacrylate (MMA) which are initially liquid and solidified after light exposure have also been applied to the extrusion-based printing [10-13]. However, the temperature of these inks during photopolymerization is much higher (~80°C) than that of normal human body (37°C), making incorporation and preservation of the bioactivity of heat-labile biomolecules (e.g. growth factors, cytokines, DNA) during the photocrosslinking process impossible [14, 15]. Moreover, these polymers are non-degradable, with potential long-term biocompatibility problems. Other photocrosslinkable inks with limited temperature elevation like gelatin methacrylate (GelMA) [16, 17], methacrylated alginate [18], methacrylated hyaluronic acid [13] and poly(ethylene glycol) dimethacrylates (PEGDMA), however, have too low mechanical properties (compressive modulus less than 1 MPa) to provide structural support for

bone regeneration [19, 20]. Furthermore, all of the above-mentioned polymers suffer from limited osteoconductivity and osteoinductivity.

To endow polymers with improved osteogenic activity and mechanical properties for better bone repair, inorganic fillers, e.g., hydroxyapatite (HA) have been employed due to its chemical similarity to natural bone mineral [8, 21, 22]. Unfortunately, the consideration of the interfacial interaction between the nanofiller and the host materials is still lacking, which may result in the inhomogeneous HA dispersion and undesirable aggregation within the polymer matrix. This may further cause nozzle clogging during printing and compromise the mechanical properties of the resultant composites [23]. Therefore, the bone tissue engineering field calls for a nanocomposite ink with superior printability, robust mechanical properties and favorable bioactivity.

In this study, we develop a photocrosslinkable nanocomposite ink consisting of tri-block poly (lactide-*co*-propylene glycol-*co*-lactide) dimethacrylate (P_mL_nDMA) and hydroxyethyl methacrylate (HEMA)-functionalized nanohydroxyapatite (nHAMA) (**Fig. 1**A). Propylene glycol is used to endow injectability/printability to the monomer, lactide for degradability and methacrylate for photocrosslinkability. The reactive HEMA-conjugated nHAMA is designed (1) to increase the stability and dispersity of the nanofiller and prevent the precipitation of the nanofillers; (2) to covalently crosslink with the surrounding P_mL_nDMA polymer matrix to form an inorganic-organic co-crosslinked nanocomposite network and further enhance the nanocomposite mechanical properties (**Fig. 1**B); (3) to buffer the acidic degradation products of the polymer and (4) to endow the nanocomposite with osteoconductivity and osteoinductivity. As expected, we find that the nHAMA can rapidly photocrosslink with P_mL_nDMA within 140 seconds and form an inorganic-organic co-crosslinked nanocomposite network, significantly enhancing the nanofiller-matrix interfacial compatibility and in particular the nanocomposite mechanical properties (modulus increased by 10-fold compared to naked polymer). By simply changing the chain lengths of PPG and LA in the P_mL_nDMA (i.e., m and n) and the content of nHAMA, we can robustly tune the rheological property, wettability, degradation, and printability of the materials. Importantly, thanks to the low exothermic heat generation (< 37°C) during photocrosslinking, our nanocomposite ink was more applicable to encapsulation and long-term release of heat-labile biomolecules (e.g., bone

morphogenic protein-2 (BMP-2)) than conventional polymer bone inks like PCL or PLGA that involves toxic organic solvents or harsh hot-melt extrusion during 3D printing [8, 9]. Together with its superior biological performances in supporting the *in vitro* and *in vivo* osteogenesis, we envision that our nanocomposite material holds great promise as bone ink for 3D printing or injectable material for bone tissue regeneration.

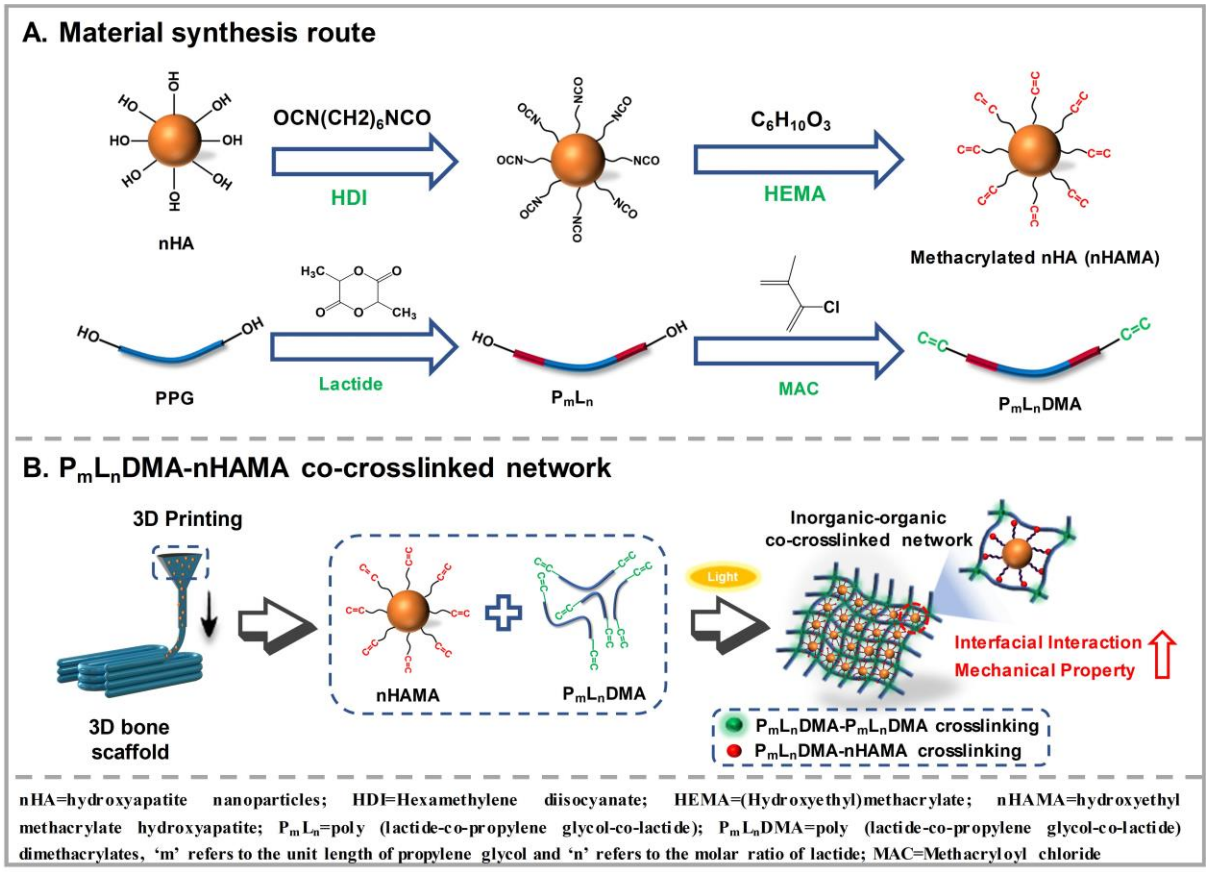

Fig. 1. Schematic illustration of (A) synthesis route of photocrosslinkable nanocomposites consisting of P_mL_nDMA and nHAMA, and (B) 3D printing of bone scaffolds with P_mL_nDMA/nHAMA nanocomposites. The nHAMA with reactive HEMA chains was designed to covalently interact with P_mL_nDMA and form an organic-inorganic co-crosslinked network within the nanocomposite, which was expected to improve the nanofiller-matrix interfacial compatibility and further enhance the mechanical strength.

2. Materials and methods

2.1 Synthesis and characterization of photocrosslinkable P_mL_nDMA

In P_mL_nDMA, 'm' refers to the unit length of propylene glycol (PPG; Sigma-Aldrich, Hong Kong), and 'n' refers to the molar ratio of lactide (LA; Sigma-Aldrich, Hong Kong) to PPG. We prepared two polymers with different chain length of PPG and LA blocks in present work: $P_{17}L_4$DMA and P_7L_2DMA with molecular weights of PPG at 1000 (m=17) and 425 (m=7) g/mol, and LA-to-PPG ratios at 4 (n = 4) and 2 (n = 2), respectively. Take $P_{17}L_4$DMA as an example. Briefly, 40 g PPG reacted with 23 g LA via a ring-opening polymerization reaction using stannous octoate (Macklin Reagent, China) as the catalyst for 6 hours at 150°C under nitrogenic environment [24, 25]. Methacrylate groups were then conjugated to the terminal end of the polymer chain by dropwise adding 4.22 g methacryloyl chloride (MAC; Macklin Reagent, China) and 4.05 g trimethylamine (TEA; Macklin Reagent, China) at 0°C, both of which were diluted in dichloromethane (DCM; Duksan, Hong Kong). To remove the resultant TEA·HCl, the product was dissolved in 200 mL of diethyl ether (Duksan, Hong Kong) followed by vacuum filtration, and finally washed with 200 mL deionized water. The final oil solvent phase was retracted from the mixture by a separatory funnel followed by 2 hours of rotary evaporation to completely remove the residual solvent. The synthesized polymers were then characterized by ^{1}H NMR on a Varian 500 MHz solid-state spectrometers (Palo Alto, USA) using deuterated chloroform ($CDCl_3$) solvent at 25°C [26]. The obtained spectra were then analyzed by the Mnova software (Mestrelab Research, Spain). The integration of the peak areas indicated the levels of specific chemical groups within the molecule. To further confirm the success of material synthesis, we additionally performed an attenuated total reflectance Fourier transform infrared (ATR-FTIR) (Thermo Nicolet iS5, US) to identify specific chemical bonding [26].

2.2 Synthesis and characterization of nHAMA

nHAMA with reactive brushes was prepared by grafting hydroxyethyl methacrylate (HEMA; Sigma-Aldrich, Hong Kong) to the surface of nHA (Macklin Reagent, China), where the hexamethylene diisocyanate (HDI; Sigma-Aldrich, Hong Kong) was used as a coupling agent [27]. Briefly, 20 g nHA was thoroughly dried at 120°C for 48 hours before dispersing in 300 mL dimethyl formamide (DMF; Duksan, Hong Kong) under nitrogen protection. 4 mL (25 mmol) HDI and 0.4 mL (0.6 mmol) dibutyl-tindilaurate as catalyst (Sigma-Aldrich, Hong Kong) were then added and left for reaction at 50°C for 24 hours. Then, 8 mL (66 mmol) HEMA was added for further reaction under the same condition for 5 hours. Finally, 400 mL methanol (Duksan, Hong Kong) was added to stop the reaction. The HEMA-grafted nHA was then

separated by centrifugation and thoroughly washed with DCM and dried at room temperature for 96 hours.

The non-grafted nHA and grafted nHAMA were characterized using ATR-FTIR to verify the coupling of HEMA chain to the nHA surface with 650-4000 cm^{-1} recording range, 2 cm^{-1} resolution and 64 scans per test. Both nHA and nHAMA were applied directly to the ATR-FTIR measurements [28]. The crystallinity of the nHA or nHAMA were measured by X-ray diffractometer (XRD, Rigaku, Japan). Cu Kα radiation (40 kV, 30 mA) was used for the measurement with scanning rate of 0.05°/s in the 2θ range from 20° to 60°. The standard cards (JCPDS No. 09-432 for pure hydroxyapatite) was used for analyzing the XRD pattern [28]. The grafting efficiency was calculated by the thermogravimetric analyzer (TGA; Mettler Toledo, US). The analysis temperature was set from room temperature to 1100°C with an increase rate of 5°C/min in the nitrogen atmosphere. Around 20 mg nHA or nHAMA was put into an alumina crucible for measurement [29]. The transmission electron microscope (TEM, JEOL Model JEM-2010, Japan) analysis of the nHA or nHAMA was performed to observe the size and morphology of the non-grafted nHA and the grafted nHAMA. The dispersed nHA or nHAMA in dichloromethane (DCM) (0.5 g/L) was sonicated for 15 min and 100 μL of the suspension was dropped on the 200-mesh copper grid coated with carbon followed by thoroughly drying in the air. The acceleration voltage was set at 80 kV [29]. The equivalent average hydrodynamic diameter and size distribution of nHA or nHAMA in ethonal (0.5 g/L) suspension were measured by dynamic light scattering (DLS). The DLS analysis based on scattering intensity of the nHA or nHAMA suspension was conducted immediately or after 30 min silencing with 15 min ultrasonic treatment. Zetasizer-Nano ZS (Malvern, UK) equipped with 4 mW He-Ne monochromatic laser source (633 nm wavelength) and avalanche photodiode detector was used. All measurements were performed at 25°C in glass cuvettes. The scattering angle was set as 90° and the duration was set as 50 second. The Malvern Zetasizer software was applied to process and analyze the data in which non-negative least square (NNLS) algorithm was used to fit the time-domain correlation function decays. For each sample, three DLS measurements were performed [30].

2.3 Fabrication of P_mL_nDMA/nHAMA nanocomposites

The P_mL_nDMA/nHAMA nanocomposites were prepared by photo-polymerization from the initial mixture consisting of P_mL_nDMA precursor solution and nHAMA. First, to prepare the P_mL_nDMA precursor solution, $P_{17}L_4$DMA or P_7L_2DMA was mixed with Irgacure 819-

containing HEMA solution (10 wt.% of Irgacure 819 in HEMA) at 9:1 (w/w) ratio. Subsequently, the desired amount of nHAMA (30, 50 and 70 wt.%) was dispersed in the polymer precursor solution and thoroughly mixed by a homogenizer. For example, 100 g of P_7L_2DMA/50%nHAMA composite consisted of 50 g of nHAMA, 45 g P_7L_2DMA, 4.5 g HEMA and 0.5 g Irgacure 819. Subsequently, the desired amount of nHAMA (30, 50 and 70 wt.%) was dispersed in the polymer precursor solution and thoroughly mixed by a homogenizer. Finally, the cylindrical-shaped nanocomposites were obtained by injecting P_mL_nDMA/nHAMA mixtures into a circular Teflon mold (Ø 6 mm×3 mm), and then photocrosslinking under a UV lamp (wavelength of 365 nm and intensity of 5 mW/cm^2, Analytikjena, Germany) for 200 seconds at room temperature. For comparison purpose, the P_mL_nDMA/nHA nanocomposites with different concentrations of nHA (30, 50 and 70 wt.%) were also prepared using the same method.

2.4 Physical characterization of P_mL_nDMA/nHAMA nanocomposites

2.4.1 Photocrosslinking kinetics

Photocrosslinking process of the P_mL_nDMA/nHAMA nanocomposites was analyzed based on the ATR-FTIR spectra. The strong intensity of the peak at 1640 cm^{-1} ascribed to the symmetric stretch of 'C=C', which reflected the photo-polymerization and was expected to disappear in the post-crosslinking spectra if complete polymer crosslinking occurred. Thus, after correction and normalization by peaks at 2940 cm^{-1} in FTIR spectra, the changes in peak height at cm^{-1} were used to quantify the polymerization ratio (R_p) after UV irradiation. The R_p was calculated according to the following equation: $R_p(\%) = \frac{H_0 - H_1}{H_0} \times 100\%$, where H_0 is the initial relative intensity of 'C=C', and H_1 is the relative intensity of 'C = C' after photocrosslinking. To trace the photocrosslinking process, the changes in the R_p after exposure of nanocomposites to UV light for different time points (0, 10, 30, 60, 90, 120 and 140 s) was also recorded.

2.4.2 Volumetric shrinkage

The volumetric shrinkage of the materials was evaluated with a linometer (ACTA, Netherlands). Briefly, 1 mL freshly prepared specimen was positioned between a glass slide and an aluminum disc with grease coating. The displacement of the aluminum disk was monitored by a non-contact probe. Then, the UV radiation (5 mW/cm^2) was implemented for 4 min at 25±1℃ on top of the glass slide to crosslink the specimen. The dynamic linear

shrinkage was collected for 10 min to exclude the influence of any thermal expansion resulted from the exothermic reaction. Finally, the linear shrinkage and volumetric shrinkage were calculated with the equations as described previously, $\text{Lin\%} = (\frac{\Delta L}{L+\Delta L})\times 100$; $\text{Vol\%} = 3\text{Lin\%} - 0.03(\text{Lin\%})^2 + 0.0001(\text{Lin\%})^3$, where ΔL is the collected displacement from the linometer, and L is the thickness of the specimens after photocrosslinking [31].

2.4.3 Thermal profiling during photocrosslinking

A compact infrared thermal camera (FLIR, US) with ±5% accuracy was used to monitor the temperature change during the photocrosslinking. The camera was positioned 0.2 m above the culture dish (60 mm diameter) in which 3 mL prepared P_7L_2DMA or $P_{17}L_4$DMA was filled. The HEMA and blank dish were used as positive and negative controls, respectively. After UV radiation started, the thermal images were captured every 5 second until the maximum temperature was reached.

2.4.4 BMP-2 release

To evaluate the capability of our nanocomposites in encapsulation and sustained release of fragile growth factors, we used the recombinant human BMP-2 (Bioss, China) as the model growth factor and incorporated it in different nanocomposites by simple blending. Briefly, 300 μg BMP-2 dry powder was thoroughly mixed with 5 g different nanocomposites, followed by casting into a disk with a diameter of 10 mm. After photocrosslinking under UV light following the above protocol, the BMP-2-containing nanocomposites were incubated in a tube containing 10 mL PBS at 37°C. At different predetermined time points, 5 mL of PBS was collected from the incubation medium that was then replenished with the same volume of fresh PBS. The released BMP-2 amount in the collected PBS was determined by the BMP-2 ELISA Kit (Bioss, China) according to the manufacture's protocol. To evaluate the bioactivity of the released BMP-2, we used the P_7L_2DMA as the model material and verify the bioactivity of the released BMP-2 using the alkaline phosphatase (ALP) staining and activity assay. Briefly, the same BMP-2-containing P_7L_2DMA nanocomposites were prepared and incubated in 100 mL osteogenic medium (Cyagen, Hong Kong) at 37°C for 7 days based on the previous BMP-2 release profile. The collected osteogenic medium was denoted as "extraction medium" and the released BMP-2 concentration in the extraction medium was determined using the BMP-2 ELISA Kit. The fresh osteogenic medium without BMP-2 was used as blank group. For the positive control group, the fresh osteogenic medium was supplemented with fresh BMP-2 to

ensure its final BMP-2 concentration was the same as that in the extraction medium (denoted as "Blank+BMP-2" group). Then, rabbit mesenchymal stem cells (rMSCs; Cyagen, Hong Kong) were seeded onto the tissue culture plate (TCP) at a density of 2×10^4 cells/cm^2 and cultured with different medium including the osteogenic medium (Blank), extraction medium, osteogenic medium with fresh BMP-2 (Blank+BMP-2), respectively. After culture for 3 and 7 days, the intracellular ALP activity was determined by ALP activity assay (Beyotime, China) normalized by the total protein content following the manufacturer's protocol.

2.4.5 Surface morphology, wettability and degradation properties

The morphology of the nanocomposites was observed using scanning electron microscopy (SEM; Tescan VEGA3, Czech Republic). Surface wettability was analyzed by measuring the static contact angle of distilled water droplets on the substrate surface using a standard water contact angle goniometer (Rame-hart, USA). The contact angle was characterized by measuring the angle between the line of the horizontal substrate surface and the tangent line of the liquid droplet to the horizontal line at the contacting point [32]. The *in vitro* degradation properties of the nanocomposites were tested in deionized water at 37°C. Each disc-shaped specimen was lyophilized and weighed using an analytical balance (Mettler Toledo, UK), prior to dipping into a 15 mL centrifuge tube containing 10 mL of deionized water. After incubation for different time periods (up to 8 weeks), the specimens were removed from the solution and gently rinsed in distilled water before being completely dried with a vacuum drier at room temperature. The relative loss of mass (M_L) at each time point was calculated according to the equation below: $M_L(\%) = \left(\frac{M_0 - M_t}{M_0}\right) \times 100$, where M_0 was the initial dry weight of the nanocomposites, and M_t was the dry weight of the nanocomposites at the preset time point. After each degradation test, the pH value of the residual solution in the tube was also measured using a pH meter (Leici, China) from day 1.

2.4.6 Mechanical properties

We performed both tensile and compressive tests to characterize the mechanical properties of the crosslinked nanocomposites. The bulk tensile properties were tested on a biaxial testing machine (MTS, US). All specimens with dimensions of 20 × 5 × 1 mm (length × width × height)

were loaded onto the testing machine, and the tensile test was performed at room temperature with a speed of 1 mm/min until specimen failure. Before the test, a metal pin was used to fix the specimens onto the apparatus. For the compression test, the specimens (Ø 6 × 3 mm) were tested on the same machine following the established protocol [33]. All specimens were compressed at a speed of 1 mm/min at room temperature until specimen failure. Four parallel specimens were tested for each material formulation to ensure reproducibility. The energy absorbed per unit volume (W) during fracture was calculated from compressive stress (σ)-strain (ε) curves using the following equation: $W = \int \sigma d\varepsilon$.

2.4.7 Rheology and printability

The viscoelastic properties of the nanocomposites were tested by a rheometer (Anton Paar, Austria) with parallel-plate (50 mm diameter and 1 mm gap width) at room temperature. Firstly, the viscosity measurements were conducted under the rotational test mode, and the shear rate ranged from 1 to 100 s^{-1}. Then, real-time rheological monitoring was carried out under the oscillation mode with 1% shear strain and 10 Hz frequency. After the modulus of nanocomposites became steady, the UV light (wavelength: 365 nm, OmniCure S2000, UK) was turned on to crosslink the nanocomposites. The storage modulus (G') was monitored in real-time as a reflection of the physical states of the nanocomposites during photo-polymerization [34]. To test the printability of the nanocomposites, 3D printing was performed using an ALPHA-CPD1 3D Bioprinter (SunP Biotech, Beijing) equipped with a motor-driven extrusion head and a simultaneous UV light source (wavelength of 365 nm and intensity of 5 mW/cm^2). The 3D models for printing were designed using Solidworks software (Dassault, France) and then converted to the 3D printer. After optimization of the printing settings, the optimal parameters (layer height of 150 µm, line width of 300 - 1200 µm, retraction distance at 1 mm and printing speed at 5-10 mm/s) were chosen to print the P_7L_2DMA/50% nHA and P_7L_2DMA/50% nHAMA nanocomposites.

2.5 *In vitro* biological characterizations of nanocomposites

2.5.1 Cell viability and morphology

Different disc-like nanocomposite samples with a diameter of 10 mm and a thickness of 2 mm were first prepared using a similar method described above. Then, these samples were disinfected through immersion in ethyl alcohol solution (70%, v/v), washed using sterile phosphate-buffered saline (PBS; Gibco, Hong Kong), and sterilized under UV irradiation for

60 min. The biocompatibility of the nanocomposites was analyzed by seeding rabbit mesenchymal stem cells (rMSCs; Cyagen, Hong Kong) onto the top surface of nanocomposites in a 24-well plate (5,000 cells/cm^2). 1 mL of complete culture medium composed of 89 vol.% Minimum Essential Medium α (MEM α; Gibco, Hong Kong), 10 vol.% fetal bovine serum (FBS; Gibco, Hong Kong) and 1 vol.% penicillin/streptomycin (PS; Gibco, Hong Kong) was added into each well. The samples were cultured in an incubator with 5% CO_2 at 37°C, and the culture medium was replaced every two days [35]. After culture for 1, 3 and 5 days, cell viability was determined using the Live/Dead assay kit (Thermo Fisher, Hong Kong) based on the manufacturer's protocol. The number of live (green) and dead cells (red) were quantified by ImageJ software. Cell viability was calculated as the ratio of live cells to total cells using 6 randomly chosen images in each sample. To examine the cell morphology on different samples, we performed F-actin staining following the manufacturer's instruction. Briefly, after culture for 1 day, cells were fixed with 4% paraformaldehyde in PBS for 15 min, permeabilized 15 min in blocking buffer (Thermo Fisher, Hong Kong) and incubated 30 min with Alexa Fluor™ 488 phalloidin (1:1000, Thermo Fisher, Hong Kong). Cell nuclei were stained with DAPI (4´,6-diamidino-2-phenylindole, 1:2000, Thermo Fisher, Hong Kong) for 10 min. 10 representative cells were selected to measure their area using Image J software according to reported protocol [36].

2.5.2 Cell proliferation

Cell proliferation was tested using Picogreen® DNA quantification assay (Thermo Fisher, Hong Kong) after culture for 1, 3, and 5 days [17]. Briefly, after removing the culture medium, samples were washed by PBS and incubated with 500 μL of proteinase K solution (50 mg/mL) at 37℃ for 2 hours for cell lysis. Then, the mixture was centrifugated at 4℃ and 14,000 rpm for 10 min. 100 μL of supernatant and 100 μL of PicoGreen® working solution (1:200 in Tris-EDTA buffer) were mixed for 5 min at room temperature. Lastly, the PicoGreen−DNA complex was detected using a fluorescence microplate reader (BioTek, US) at the excitation and emission wavelengths of 485 and 530 nm, respectively. The total amount of DNA in the sample was calculated using a standard curve according to the manufacturer's protocol.

2.5.3 Osteogenic differentiation

Alkaline phosphatase (ALP) and Alizarin Red S (ARS) staining were performed to confirm the osteogenesis of the rMSCs on the samples (Ø10 mm×2 mm) [37]. The rMSCs were seeded at

a density of 2×10^4 cells/cm^2 and cultured using the osteogenic medium (Cyagen, Hong Kong). After culture for 0, 3, 7 and 14 days, the intracellular ALP activity was determined by ALP activity assay (Beyotime, China) normalized by the total protein content following the manufacturer's protocol. Simultaneously, ARS staining for mineralized bone nodule formation was carried out by firstly fixing rMSCs in 4% paraformaldehyde for 10 min prior to being washed with PBS. Then, ARS solution (Solarbio, China) was added and incubated for 15 min. After that, the samples were washed repeatedly with deionized water to remove the weakly adhered ARS, and then imaging was performed using microscopes (Nikon, Japan). For quantification, the stain was dissolved with 10% cetylpyridinium chloride (Sigma, USA) for 3 hours at room temperature. The absorbance of the ARS extracts was measured at 592 nm using a microplate reader (BioTek, US).

2.5.4 Calcium ion release

The release of calcium ion from P_7L_2DMA, P_7L_2DMA/30%nHAMA, P_7L_2DMA/50%nHA, P_7L_2DMA/50%nHAMA were measured by Inductively Coupled Plasma Optical Emission Spectrometry (ICP-OES, Agilent). Briefly, different samples (weight: 200 mg) were incubated in PBS at 37°C. Then, at different time points, 50 μL of the conditioned PBS was collected, followed by dilution to 2 mL for ICP-OES analysis. At the same time, 50 μL fresh PBS was supplemented to continue the test.

2.5.5 Quantitative assay of gene expression

The gene expressions of osteogenesis-related markers (Runt-related transcription factor 2 (Runx2), collagen type I (Col-1), osteocalcin (OCN) and ALP) and mechanosensing-related markers (Integrin α_2, focal adhesion kinase (FAK), extracellular-signal-regulated kinase 1 and 2 (ERK1 and ERK2)) were measured using quantitative reverse transcription-polymerase chain reaction (qRT-PCR). Briefly, rMSCs were seeded onto different nanocomposites (diameter: 10 mm) at a density of 2×10^4 cells/cm^2 and cultured for 7 days. Then, cells were collected from each group, and the total RNA was extracted using Total RNA Kit (Omega, Hong Kong). 1 μg of total RNA was reverse-transcribed to complementary DNA (cDNA) using the PrimeScript RT Master Mix Kit (Takarabio, Hong Kong). qRT-PCR was performed by the Real-Time PCR Detection System with TB Green Premix Ex Taq Kit (Takarabio, Hong Kong) under the conditions of 5 seconds at 95°C, 30 seconds at 60°C, and the fluorescence intensity was recorded for 40 cycles. The $2^{-\Delta\Delta CT}$ method was adopted for quantification of the relative

expression of each interested genes, and GAPDH as the housekeeping gene was used as the internal control [38]. The primer sequences of each gene utilized for PCR amplification were listed in Table S1.

2.6 *In vivo* biological characterizations of nanocomposites

2.6.1 Rabbit femoral condyle defect animal model

All animal procedures were approved by the Ethics Committee of the Hong Kong Polytechnic University. A total of 48 male New Zealand white rabbits (19-20 weeks, 3-3.5 kg) were used and randomly divided into four groups (blank, P_7L_2DMA/50%nHA, P_7L_2DMA/50%nHAMA and P_7L_2DMA/50%nHAMA/BMP-2). For fabrication of P_7L_2DMA/50%nHAMA/BMP-2 scaffold, 300 μg BMP-2 dry powder was employed and thoroughly mixed with 5 g P_7L_2DMA/50%nHAMA nanocomposites prior to 3D printing. Then, we detected the morphology and pore size of all the printed scaffolds by using SEM and micro-CT (SkyScan, Belgium) with 9 μm resolution, 1 mm aluminum and copper filter and 80 kV voltage. Next, rabbits were firstly anesthetized by intramuscular injection of pentobarbital sodium. Then, we made a 5 cm longitudinal skin incision, dissected the shin and musculature at the lateral femoral and exposed the femoral condyle. A defect with the diameter of 6 mm was created on femoral condyle using a dental drill and subsequently implanted with the scaffold (6 mm in diameter and 5 mm in height). The defect left untreated served as the blank control. Finally, the muscle and skin of the rabbits were sutured, and the animals were intramuscularly injected with antibiotics for 3 days and raised freely in cages.

2.6.2 Micro-CT evaluation

After 4 and 8 weeks post-surgery, six rabbits from each group were sacrificed using CO_2 suffocation. The femur specimens were harvested and scanned using Micro-CT scanner (SkyScan, Belgium) with the following settings: 9 μm resolution, 0.5 mm aluminum and copper filter, and 80 kV voltage. The scanning data were further processed by the Micro-CT software to reconstruct 3D images. Morphometry data including the bone mineral density (BMD) and bone tissue volume/total tissue volume (BV/TV) in the region of interest (ROI) were quantitatively analyzed based on micro-CT reconstruction data.

2.6.3 Histological observation

After micro-CT analysis, the histology analysis was further performed by Van Gieson's picrofuchsin staining to observe the formation of new bone tissues in the defect sites. The femur specimens were first fixed in 4% paraformaldehyde for 48 h, and then dehydrated and soaked in poly(methyl methacrylate) (PMMA) solution for 3 weeks. After solidification, sections of each specimen were prepared using a diamond saw, and then stained with Van Gieson's stain and observed under a light microscope (Nikon, Japan). The percentage of the newly formed bone was analyzed by the ImageJ software.

2.7 Statistical analysis

All measurements were carried out at least in triplicate if not specified. The quantitative data were expressed as mean ± standard deviation (SD). Normality testing was first performed using the Shapiro-Wilk test. If the data were normally distributed, Student's t-test and one-way analysis of variance (ANOVA) were adopted for two-group comparation and multi-group comparation (more than two groups), respectively. For the one-way ANOVA, Tukey post-hoc test was then performed for evaluations of differences between specific groups. In our study, variance between groups was found to be equal using Levene's test. For the non-normal distributed data, non-parametric statistical tests were chosen, where Wilcoxon Signed rank test was adopted to detect the statistical significance of two-group differences, while Kruskal-Wallis test was used for comparation of more than two groups. In all statistical evaluations, A p value of < 0.05 was considered statistically significant.

3. Results and discussion

3.1 Characterizations of P_mL_nDMA and nHAMA

In this study, we developed a robust photocrosslinkable nanocomposite ink for bone repair. As shown in **Fig. 2**A, the ^{1}H NMR spectra confirmed the successful synthesis of P_mL_nDMA. In the spectra of P_mL_n (P_7L_2 and $P_{17}L_4$), the broadened peaks at ~3.54 ppm were attributed to the protons adjacent to original '-CH_2' and '-CH' groups in the PPG, while the peaks at ~5.11 ppm and ~4.35 corresponded to the proton in linear '-CH' group and the '-CH' group adjacent to the terminal '-OH' group in the LA chain, indicating the conjugation of LA to PPG. For the spectra of P_7L_2DMA and $P_{17}L_4$DMA, distinctive peaks in the double bond region (~5.6 ppm and ~6.21 ppm) appeared, suggesting the methacrylation of P_mL_n. (**Fig. 2**A). The FTIR spectra also revealed the synthesis process of P_mL_nDMA by first coupling the LA group to the PPG and then conjugating the methacryloyl group to the intermediate products P_mL_n (**Fig. S1**).

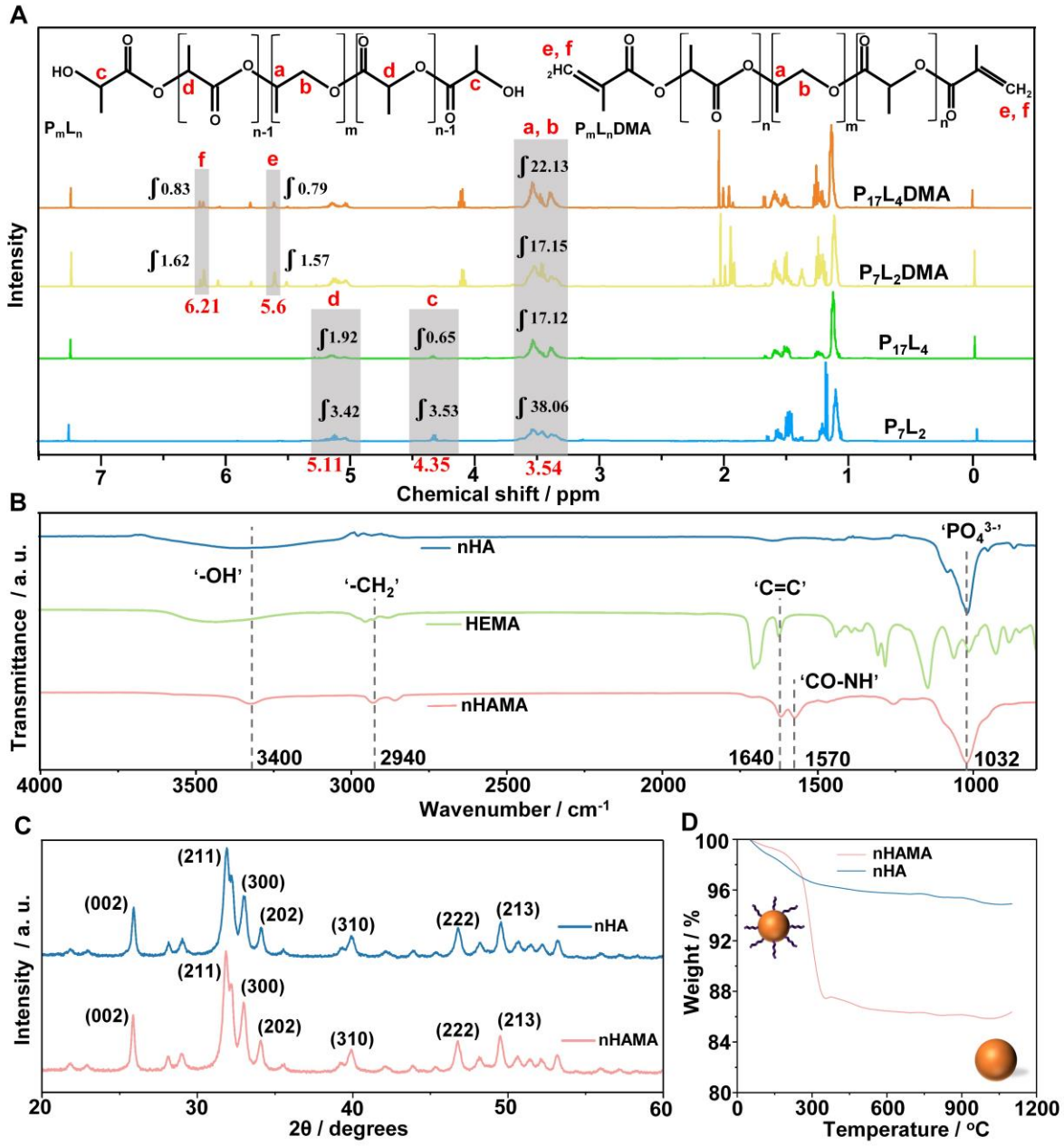

Fig. 2. Characterization of P_mL_nDMA and nHAMA. (A) ^{1}H NMR spectrum of P_7L_2, $P_{17}L_4$, P_7L_2DMA and $P_{17}L_4$DMA. "∫" denotes the integration of the resonances. (B) FTIR spectra of nHA, HEMA and nHAMA. (C) XRD analysis of nHA and nHAMA with scanning rate of 0.05°/s in the 2θ ranges from 20° to 60°. (D) TGA plots of nHA and nHAMA with temperature increase rate at 5°C /min.

nHAMA was synthesized by grafting HEMA to the surface hydroxyl groups of nHA via HDI. **Fig. 2**B demonstrated the FTIR spectra of naked nHA, HEMA and synthesized nHAMA. The characteristic peaks of nHA (3400 cm^{-1} and 1032 cm^{-1} corresponding to '-OH' and '-PO_4^{3-}' groups, respectively) in nHAMA kept almost unchanged in contrast to pure nHA [39]. After the introduction of HEMA, the characteristic peaks of HEMA (2940 cm^{-1} for '-CH_2' groups and 1640 cm^{-1} for 'C=C' groups) and HDI (1570 cm^{-1} for '-CO-NH' groups) appeared in nHAMA, confirming the successful synthesis of nHAMA. Then, we performed TGA to quantify the amount of organic phase (HDI-HEMA) grafted onto the nHAMA by comparing the differences of the total weight loss between nHA and nHAMA. The results revealed that 7.6 wt.% of HDI-HEMA was coupled to nHAMA. The crystalline structure of the non-grafted nHA and grafted nHAMA were further identified using X-ray diffraction (XRD). The XRD pattern of the nHA and the nHAMA remained almost the same with characteristic diffraction of (0 0 2), (2 1 1), (3 0 0), (2 0 2), (3 1 0), (2 2 2), and (2 1 3) without presence of crystalline phase changes or secondary phases, indicating the maintenance of crystalline nature of hydroxyapatite after the grafting reaction (**Fig. 2**C). These results confirmed that the surface modification only occurred selectively on the surface of nHA and did not alter the crystallinity, crystalline phase or the intrinsic properties of nHA. We then performed TEM to evaluate the morphology of nHA and nHAMA. Both the nHA and the nHAMA demonstrated an ellipsoidal morphology with no substantial difference (**Fig. S2**). Next, the Z-average and size distribution of nHA or nHAMA were determined using DLS. The DLS demonstrated slightly increased Z-average for nHAMA (97 nm) as compared to nHA (82 nm), which might be attributed to the formation of a hydrodynamic shell around the nHAMA by grafted HDI-HEMA chain. After 30 min silencing, there was no significant change in the Z-average or the PDI for the nHAMA; however, the nHA exhibited an obvious Z-average increase to 523 nm and much broader size distribution (PDI = 0.428), indicating the occurrence of aggregation in the nHA suspension. The above results have suggested the superior stability and dispersibility of nHAMA (**Fig. S3**). It is well-known that naked nano-HA is liable to form aggregates in the polymer matrix as a result of interparticle van der Waals forces and hydrogen bonding between surface hydroxyl groups, which may lead to non-homogeneous distribution and decrease the mechanical property and biocompatibility of the resultant nanocomposites [27]. Here, after grafting nHAMA with brushes (HDI-HEMA chain), we found that the colloid stability of nHAMA in ethanol was significantly increased compared to the naked nHA after 12 hours of immersion (**Fig. S4**). This phenomenon might be attributed to the formation of a shell shield by HDI-

HEMA brushes which reduces interparticle electrostatic interaction to prevent the aggregation of nHAMA [40]. However, when exposed to UV radiation, the nHAMA sample formed much more precipitation than nHA in the photoinitiator-containing ethanol solution as a result of photocrosslinking, demonstrating the reactivity of methacrylated moieties on nHAMA (**Fig. S4**). These results suggested that P_mL_nDMA and nHAMA were prepared successfully.

3.2 Photocrosslinking and morphology of P_mL_nDMA/nHAMA nanocomposites

To prepare the P_mL_nDMA/nHAMA nanocomposites, we blended the liquid P_mL_nDMA with nHAMA powder with different weight percent. When the weight proportion of nHAMA reached 70 wt.%, the composite materials lost their injectability with severe aggregation (**Fig. S5**). By adjusting the weight proportion to 30 and 50 wt.%, we obtained paste-like nanocomposites, which were used in the following studies. In general, a photocrosslinkable ink for extrusion-based 3D printing must solidify fast under light irradiation to form a stable filament after extrusion, ensuring the accuracy of printed structure [24, 25]. The FTIR spectra of $P_{17}L_4$DMA and P_7L_2DMA after UV illumination for 0, 30 and 60 s showed a substantial decrease of 'C=C' bond intensity with time due to the conversion of the methacrylate groups, indicating the rapid photocrosslinking of the P_mL_nDMA polymers (**Fig. S6**). To characterize the photocrosslinking kinetics of the nanocomposites, we calculated the photopolymerization ratio (R_p) of various material formulations after different UV exposure times (**Fig. 3**A and B). The photocrosslinking reactions for all formulations occurred immediately upon UV light radiation and the R_p reached as high as 50% for most nanocomposites within 20 seconds. After 140 seconds of UV exposure, the complete photocrosslinking was observed in all material formulations. Compared with pure $P_{17}L_4$DMA, P_7L_2DMA possessed a higher polymerization rate especially within the first 10 seconds. This could be attributed to the shorter polymer chain length and higher 'C=C' concentration in P_7L_2DMA, which reduced the steric hindrance for free radical diffusion and accelerated photopolymerization reaction. After incorporating nHAMA or nHA into the polymer matrix, the photocrosslinking rates of nanocomposites decreased compared to the corresponding pure polymer because of light scattering (**Fig. 3**A and B). Compared with nHA-containing nanocomposites at the same weight percent, a slight increase in photocrosslinking rate was observed in nHAMA-containing nanocomposites. Such differences might be due to the increased photo-reactivity of the material system and higher homogeneity of nHAMA within the polymer matrix, which decreased light scattering, increases light absorption and thus promotes photocrosslinking kinetics [41]. Our

results suggested the good fast-setting property for the P_mL_nDMA/nHAMA nanocomposites, guaranteeing structural integrity and high resolution for use as a composite ink in photocrosslinking-assisted extrusion-based printing.

After photocrosslinking, both $P_{17}L_4$DMA and P_7L_2DMA polymers exhibited volumetric shrinkage of 6.5 ± 0.66% and 8.6 ± 0.72%, respectively, due to the shift of long-range Van der Waals interactions to short covalent bonds between the carbon atoms of monomers (**Fig. S**7) [42]. P_7L_2DMA polymer demonstrated a significantly larger shrinkage than the $P_{17}L_4$DMA polymer as a result of shorter polymer chain length and higher 'C=C' concentration. After incorporation of the nHAMA or nHA, the volumetric shrinkage decreased with increasing solid content. The P_7L_2DMA or $P_{17}L_4$DMA nanocomposites containing 50%nHAMA or nHA showed a lowest volumetric shrinkage (< 4%), compared to other counterparts. This could be attributed to the less polymer content for shrinkage and the steric hindrance of the nHAMA or nHA particles on the shrinkage of polymer matrix. Such minor shrinkage of the nanocomposites was highly beneficial for ensuring 3D printing accuracy and shape fidelity.

Some commonly used photocrosslinkable materials such as HEMA involve the free radical-based photo-polymerization that could lead to a sharp exothermic temperature rise during crosslinking and might cause the inactivation of the loaded biomolecules [43]. **Fig. 3**C exhibited the exothermic temperature profile during the photo-polymerization of the polymers and HEMA. Remarkable temperature rise was observed in HEMA peaking at 74.9^{o}C at 70 seconds, while the peak temperatures for both P_7L_2DMA (peaking at 36.2 ^{o}C) and $P_{17}L_4$DMA (peaking at 33.5^{o}C) was significantly lower than that of HEMA. We speculated such differences in temperature rise might be triggered by the higher reactivity and concentration of "C=C" double bond in HEMA, which could lead to severe polymerization reaction and heat generation [44]. After incorporating nHA or nHAMA, we found the exothermic temperature of the nanocomposites was further reduced as a result of less polymer acting as the heat source and increased bulk heat conductivity (**Fig. 3**D and E) [45]. Currently, although some synthetic polymers such as poly(lactic acid) (PLA), poly(glycolic acid) (PGA) have been applied in delivery of growth factors, the major challenges still lay in preserving the bioactivity of growth factors during the incorporation process as well as maintaining the stability of long-term release [46]. Of note, the peak temperatures of our prepared polymers or nanocomposites were lower than the normal body temperatures (37^{o}C), suggesting their great potential in tissue engineering applications, especially in the direct encapsulation of heat-labile biomolecules.

3.3 *In vitro* release of BMP-2

Before we examined the BMP-2 release, we first observed the dispersion of nHAMA in the $P_{17}L_4$DMA or P_7L_2DMA matrix using SEM (**Fig. S8**). It was found that nHAMA was distributed uniformly on the surface of $P_{17}L_4$DMA or P_7L_2DMA without the formation of evident agglomeration. We then incorporated BMP-2 as a model drug into the nanocomposites by simple blending to investigate the drug encapsulation capability of the nanocomposites and the *in vitro* drug release profile. Since exothermic temperature of nHAMA-containing nanocomposites during photo-polymerization were almost the same as that of nHA-containing nanocomposites (**Fig. 3**D and E), we chose the nHAMA-containing nanocomposites for the BMP-2 release test. As shown in **Fig. 3**F, a sustained BMP-2 release over 60 days with no burst release occurring was observed in all groups. The BMP-2 release from $P_{17}L_4$DMA was nearly the same as that from P_7L_2DMA. Compared to pure polymer and nanocomposites containing 30% nHAMA groups, the 50%nHAMA-containing nanocomposites exhibited the fastest BMP-2 release. This may be because of the hydrophilic nature of nHAMA. As presented in **Fig. 3**G, with the increasing content of nHAMA, the hydrophilicity of the nanocomposites was improved, which might facilitate water infiltration into the polymer network, accelerating the material hydrolytic degradation and drug release. Meanwhile, we demonstrate the bioactivity of the release BMP-2 by comparing the osteogenic potential between the extract medium and the osteogenic medium adding fresh BMP-2. As shown in Fig S, the purple ALP staining colonies appeared in all groups after 3 days, and became larger and denser on day 7. Notably, compared with the blank group, the staining area and activity of ALP were significantly elevated in both “extraction medium” and the “blank+BMP-2” groups. Moreover, there was no significant difference in ALP staining and activity between the “extraction medium” group and the “blank+BMP-2” group, indicating that the released BMP-2 possessed a similar osteogenic effect to the fresh BMP-2. These results collectively verified our scaffold fabrication process is friendly to preserve the bioactivity of growth factors encapsulated in the materials. All together, our nanocomposites allowed for the facile encapsulation of growth factors to achieve a long-term, stable and slow release pattern, with great potential as the drug carriers.

3.4. Degradation properties of the nanocomposites

In vitro degradation profile of different material formulations were further evaluated in terms of mass loss versus time (**Fig. 3**H). All materials were slowly eroded with soaking period extending, and over 75% of materials remained for all groups after immersion for 8 weeks compared to the initial day. In addition, we found higher contents of nHAMA in the nanocomposites were correlated with a faster degradation rate, which was consistent with the literature [47]. The degradation kinetics of the materials were in good agreement with the above BMP-2 release characteristics, indicating that the encapsulated BMP-2 was released from materials along with matrix degradation and that the release rate was mainly dependent on the degradation rate of materials. Such slow and controllable degradation behavior that could match the new bone formation rate was believed to be considerably important for a scaffold material since the implanted scaffold is required to gradually degrade to maintain scaffold structural integrity and allow for tissue ingrowth during bone repairing [48].

Since the change of pH value during scaffold degradation significantly influences the cellular microenvironment after implantation, we also monitored the pH values of the immersion solution for all scaffolds. After 60 days' soaking, the pH of the pure $P_{17}L_4$DMA or P_7L_2DMA scaffolds decreased to 3.3-4.2 and 4.3-4.7, respectively, which was due to the release of acidic degradation products (**Fig. 3**I). However, compared with the pure polymer scaffolds, nHAMA-containing scaffolds showed significantly higher pH values with no noticeable fluctuations, suggesting that the addition of nHA into the scaffolds could effectively neutralize the acid products from P_mL_nDMA degradation, and thus maintain the pH stability of degradation medium. In short, our P_mL_nDMA/nHAMA nanocomposites exhibited a controllable degradation rate and could provide a relatively suitable cellular microenvironment for bone regeneration.

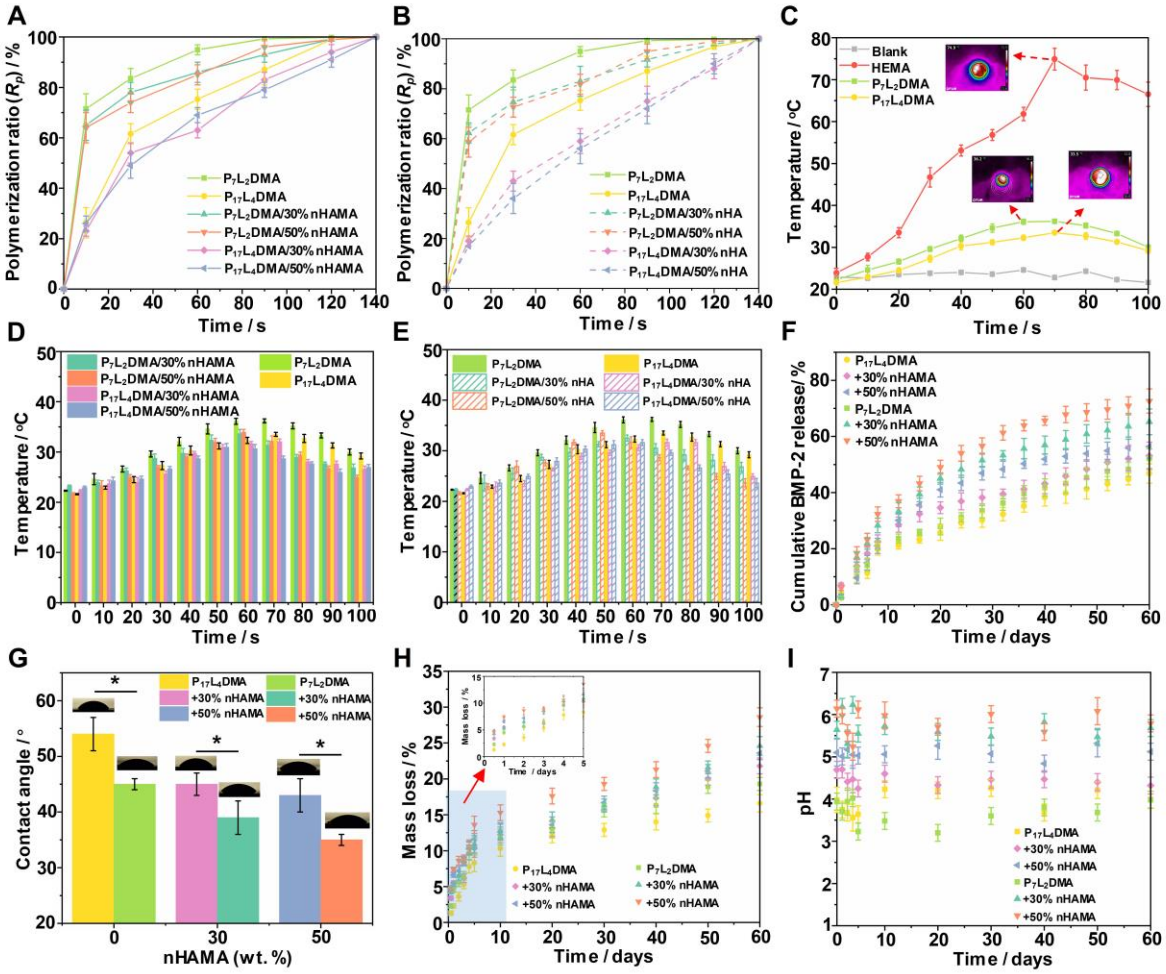

Fig. 3. Photo-polymerization ratio of the pure P_7L_2DMA and $P_{17}L_4$DMA polymers and their nanocomposites containing different contents of (A) nHAMA or (B) nHA as a function of time calculated according to the FTIR spectra. Exothermic temperature profiles of (C) $P_{17}L_4$DMA, P_7L_2DMA, HEMA, and the nanocomposites with (D) nHAMA and (E) nHA monitored using the infrared thermal camera. (F) *In vitro* cumulative release profile of BMP-2 from different material formulations after immersion in PBS for 60 days. (G) The contact angle measurements of the nanocomposites with different concentrations of nHAMA. Inserted images showed the morphology of water droplets on the material surfaces. (H) The percentage of weight loss of various material formulations along with degradation. The inserted image displayed the mass loss of materials in the first 5 days. (I) The pH change of immersion solution during scaffold degradation. Data were presented as mean ± SD and analyzed by one-way ANOVA (n = 3 for each sample, *p < 0.05).

3.5 Mechanical properties of the nanocomposites

Mechanical property is one of the most important clinical criteria for bone scaffolds. Ideally, these scaffold materials should provide adequate support and share the load with the nearby bone tissues during the regeneration of bone defect. A scaffold material with enhanced mechanical strength that matches native bone tissues is highly sought after. Besides, the elasticity and toughness are the other two critical requirements for the scaffold materials, which improve the handling ability during surgeries and withstand repetitive compressive loads, avoiding sudden fractures after implantation [4]. To comprehensively evaluate the mechanical performances of our nanocomposites, both tensile and compressive tests were conducted in this study. From the tensile and compressive stress strain curves of various material formulations, we observed a significantly enhanced mechanical strength for nHAMA-containing nanocomposites compared to the pure P_mL_nDMA or nHA-containing nanocomposites (**Fig. 4**). In detail, the tensile modulus and strength of P_7L_2DMA-based formulations were much higher than that of the $P_{17}L_4$DMA counterparts, which might be due to the denser polymer network of P_7L_2DMA (**Fig. 4**Ai-iii). After incorporation of nHA or nHAMA into P_mL_nDMA, the nanocomposites exhibited a remarkable increase in the modulus and strength compared with the pure P_mL_nDMA. As expected, the P_mL_nDMA/nHAMA nanocomposites possessed a higher tensile modulus and strength than their P_mL_nDMA/nHA counterparts. In particular, the tensile modulus of P_7L_2DMA/50%nHAMA could reach as high as 157 MPa, nearly 1.61 times as that of P_7L_2DMA/50%nHA and 10 times as that of pure P_7L_2DMA. This substantial increase in tensile capability might be resulted from the covalent bonding between the HEMA chain on nHAMA and the polymer matrix, which further increases the interfacial interaction of the organic-inorganic phase, allowing for efficient load transfer at the interface under tensile test [49, 50]. In addition, we found that the incorporation of nHA or nHAMA could lead to a slight decrease in the maximum elongation. However, compared with the P_mL_nDMA/nHA counterparts, P_mL_nDMA/nHAMA displayed a higher fracture elongation (**Fig. 4**Aiv). This is because that the addition of nanoparticles into polymer matrix could restrict the stretching and movement of the polymer chains and reduce the compliance of the polymer network, leading to a lower stretchability [49]. In contrast, in the nHAMA-loaded polymer matrix, the enhanced two-phase interface bonding could reduce the particle agglomeration and induce more even particle distribution, thus increasing matrix yield strength to endure great deformation before failure.

Similarly, the compressive properties of the materials followed the same trends as those of the tensile properties (**Fig. 4**B). The P_7L_2DMA/50%nHAMA and $P_{17}L_4$DMA/50%nHAMA

nanocomposites possessed the highest compressive modulus and strength of 363 MPa and 235 MPa, and 159 MPa and 86 MPa, respectively, representing increase of 9 times and 8 times, and 12 times and 8 times, respectively, compared with the corresponding pure polymer matrix. Such excellent compressive properties made these nanocomposites comparable to the natural cancellous bone with compressive modulus of 80-1000 MPa [20]. We also estimated the material toughness (the energy absorbed per unit volume prior to fracture) by evaluating the area under the compressive stress-strain curve. As shown in **Fig. 4**Biv, under the same weight of nanoparticle fillers, P_7L_2DMA/nHAMA and $P_{17}L_4$DMA/nHAMA absorbed much more energy and exhibited better toughness than their nHA-containing counterparts. The interface debonding and void formation is commonly the main reason for composite material failure during the compression test [51]. The higher energy absorption of P_mL_nDMA/nHAMA nanocomposites could be due to the enhanced interfacial bonding between the polymer matrix and the brushes-grafted nHAMA. Such stronger interfacial interaction enabled effective energy dissipation in the polymer matrix by evenly distributing stress to the matrix. Overall, these results suggested that P_mL_nDMA/nHAMA nanocomposites possessed excellent mechanical performances and were a promising candidate material for bone repair, especially for load-bearing bone regeneration. In combination with the results of photocrosslinking evaluation, we used the nHAMA-containing material formulations for the following studies.

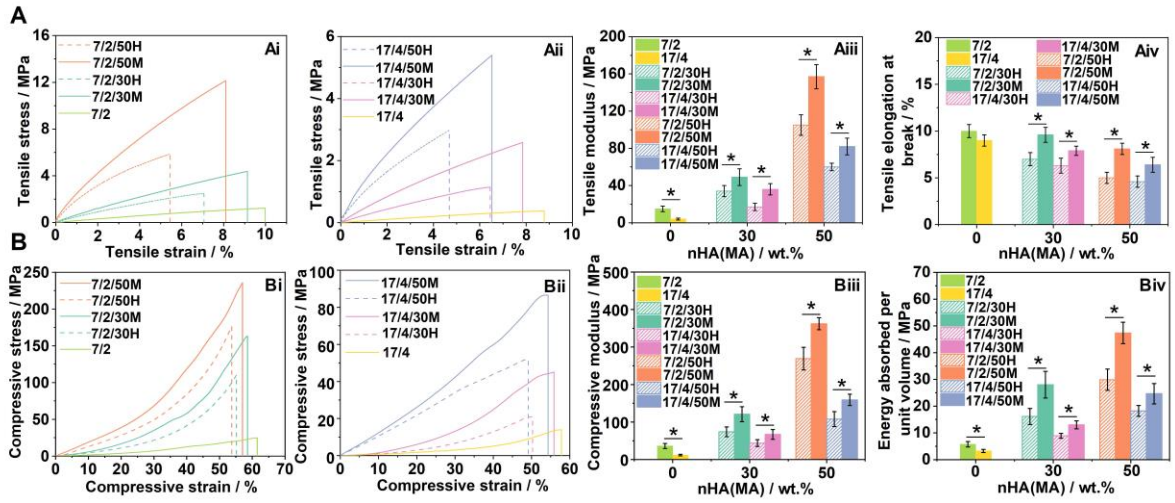

Fig. 4. The (A) tensile and (B) compressive properties of the pure P_7L_2DMA and $P_{17}L_4$DMA polymers and their nanocomposites containing different contents of nHA or nHAMA. The stress-strain curve of (Ai,ii) tensile and (Bi,ii) compressive test of different material formulations. (Aiii) The tensile modulus and (Aiv) maximum elongation in the tensile test. (Biii) The compressive modulus and (Biv) energy absorbed per unit volume in the compressive test. The 7/2 and 17/4 denoted P_7L_2DMA and $P_{17}L_4$DMA. The 30H and 30M denoted 30%nHA

and 30%nHAMA, the 50H and 50M denoted 50%nHA and 50%nHAMA, respectively. Data were presented as mean ± SD and analyzed by Student's t-test or one-way ANOVA (n = 4 for each sample, $*p < 0.05$).

3.6 Printability of the nanocomposites

Generally, a photocrosslinkable material used as an ink for extrusion-based printing should have suitable rheological properties to achieve shape reliability, that is, lower viscosity during extrusion to allow for optimal flow through the printer syringe, and higher viscosity once being deployed to maintain structural integrity [52]. To demonstrate the 3D printability of our nanocomposites, a rheological study was first conducted by measuring the viscosity as a function of shear rate. As illustrated in **Fig. 5**A, the viscosities of $P_{17}L_4$DMA-containing groups were higher than those of the P_7L_2DMA-containing groups at the same concentration of nHAMA, possibly due to the longer polymer chain of $P_{17}L_4$DMA. Both pure P_7L_2DMA and $P_{17}L_4$DMA exhibited Newtonian fluid behavior, with low and unchanged viscosities despite being applied shear rate. However, when incorporated with nHAMA, the nanocomposites displayed a shear-thinning behavior (i.e., decrease in viscosity with increase in shear rate) in the low shear rate range 0-40 s^{-1}. Notably, with increase in nHAMA content, the nanocomposites exhibited a higher viscosity and a more pronounced shear-thinning property (the viscosities of 50%nHAMA-containing nanocomposites were significantly reduced from 7 $\times 10^5$ to 1.5 $\times 10^4$ mPa·s during the measurement). Such rheological property is crucial for the nanocomposites to be used in extrusion-based printing since it ensures the ink extrudability while providing a good resolution to the final printed construct. In addition, we further performed the real-time photorheological measurement to evaluate the evolution of the storage moduli (G') with the irradiation time. The G' of all materials increased immediately upon UV irradiation, and gradually plateaued after only 140 s of irradiation, indicating a complete photocrosslinking reaction in a short time (**Fig. 5**B). Compared with pure polymer, the time for nanocomposites to reach the equilibrium of G' was prolonged slightly. This phenomenon could be explained by two aspects: (1) the reduced photo-reactivity of composite system caused by light scattering of nHAMA, and (2) the higher viscosity in nHAMA-containing formulations that restricts movement of UV-irradiated free radicals. Moreover, we found the larger the amount of nHAMA in the nanocomposites, the higher the equilibrium G' value reached, indicating the enhanced chemical interactions of nHAMA with the polymer chains contributed to the increased elastic modulus of covalently crosslinked nanocomposites. These results were

consistent with above photocrosslinking kinetics experiments, validating the excellent photocrosslinking performance and 3D printability of the nanocomposites.

Next, we evaluated the capability of printing P_mL_nDMA/nHAMA nanocomposites into various complicated 3D structures. We chose P_7L_2DMA/50%nHAMA as the ink to perform the 3D printing test due to its high viscosity. After optimizing the printing parameters, a multi-layered scaffold with a fiber diameter of ~350 μm was obtained, which demonstrated high printing resolution (**Fig. 5**C). Also, it has been verified that this nanocomposite could be printed into other complex shapes and structures (**Fig. 5**D). All in all, our nanocomposites demonstrated a desirable printability in fabrication of 3D bone scaffolds. Since the P_7L_2DMA-containing nanocomposites outperformed their $P_{17}L_4$DMA counterparts in the above physicochemical assessments, we selected the former for the following *in vitro* biological studies.

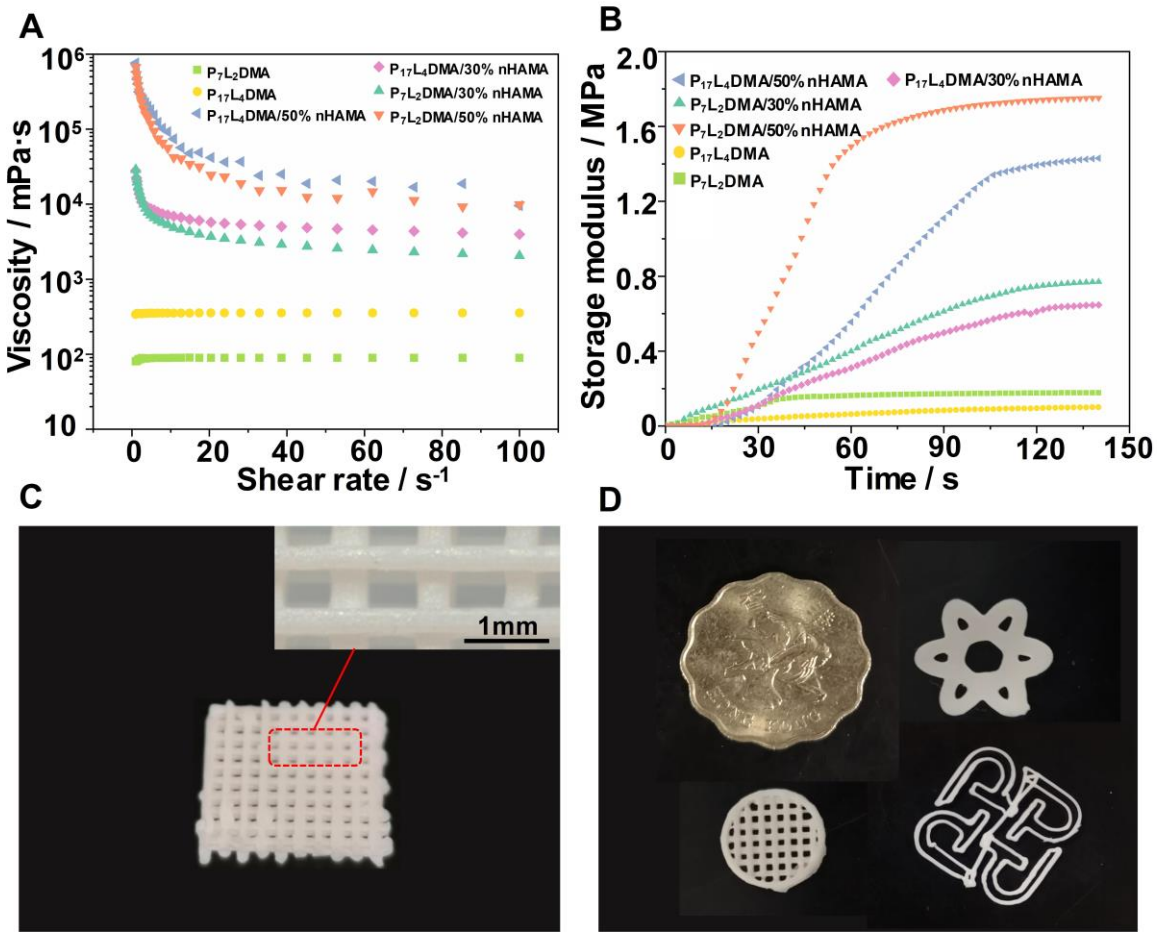

Fig. 5. Rheology and printability evaluation of the nanocomposites. (A) The viscosity versus shear rate profile of P_7L_2DMA and $P_{17}L_4$DMA with/without 30 or 50 wt.% nHAMA. (B) Real-time rheology profile of different material formulations after light exposure. Images of (C) a

multi-layered scaffold, and (D) various 3D shapes and structures printed with P_7L_2DMA/50%nHAMA nanocomposites.

3.7 *In vitro* biological evaluation of nanocomposites

3.7.1 Cytocompatibility

The biocompatibility of the scaffolds is a fundamental requirement for their successful applications in tissue engineering. Here, we first characterized the cytocompatibility by seeding rMSCs onto the P_7L_2DMA samples containing different contents of nHAMA or nHA. After 1 day of culture, the rMSCs in all groups distributed evenly on the material surface. Among these groups, cells on the P_7L_2DMA/50%nHAMA seemed to display elongated and polygonal morphology with significantly larger cell area compared to other groups, indicating the capability of our materials to boost cell adhesion (**Fig. 6** A and C). After culture for 3 days, Live/Dead staining showed that most of the cells stayed alive, with the cell viability reaching as high as 90% during the culture period (**Fig. 6**B and D). We then evaluated the cell proliferation by examining DNA concentrations that were in direct proportion to cell numbers. As shown in **Fig. 6**E, the cell numbers increased over time for all groups. The nanocomposites containing 50%nHAMA and 50%nHA presented significantly higher DNA concentrations than the pure P_7L_2DMA group after 3 and 5 days of incubation; however, there was no significant difference between the 50%nHAMA and the 50%nHA groups. Thus, we speculated that the cell proliferation was less likely to be affected by the mechanical modulus of the composites. In contrast, due to the hydrophilic nature of nHA/nHAMA, we considered the enhanced surface hydrophilicity with increasing nHA/nHAMA content would be the dominate factor that provided a suitable microenvironment for cell proliferation. These results suggested our nanocomposites exhibited satisfactory cytocompatibility and could support cell adhesion and growth after implantation.

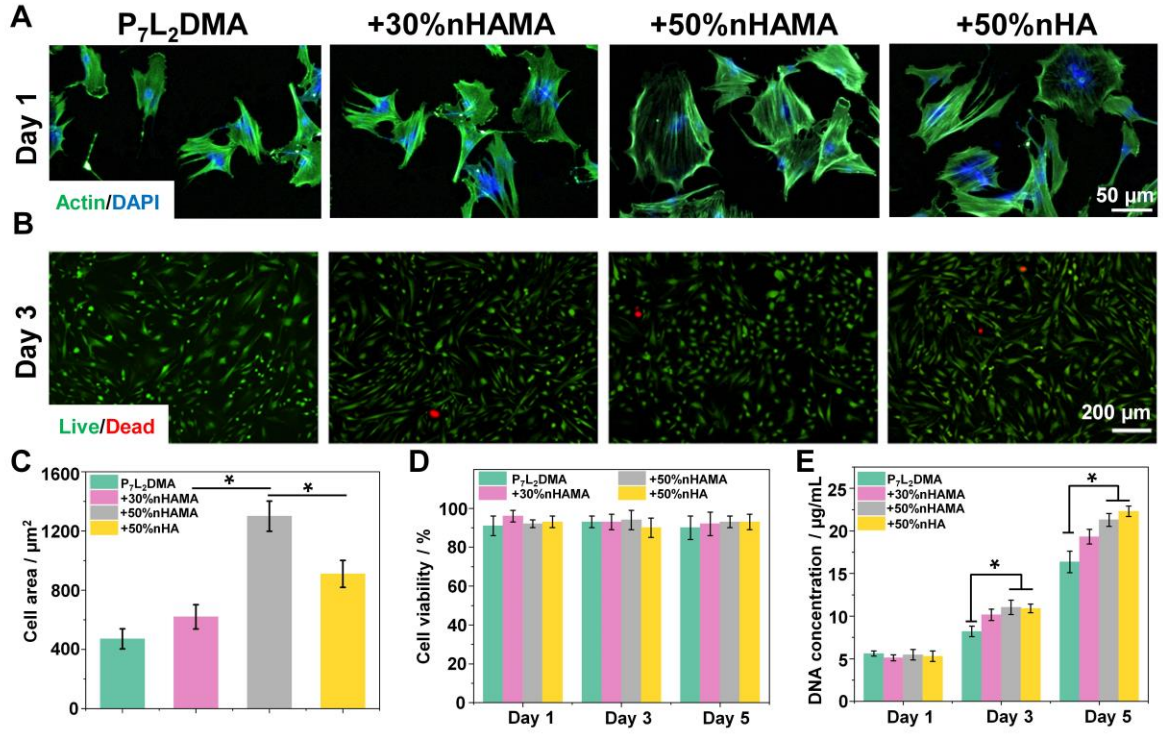

Fig. 6. Cytocompatibility of different material formulations by co-culture with the rMSCs for 1, 3 and 5 days. (A) Cell adhesion on different material surface at day 1. Green fluorescence indicated cell filaments and blue fluorescence indicated cell nuclei; (B) Live/Dead staining at day 3. Green fluorescence indicated viable cells and red fluorescence indicated dead cells; (C) Quantification of the cell area on different material surface at day 1; (D) Quantitative analysis of cell viability based on Live/Dead staining. (E) Cell proliferation measured using the Picogreen® DNA quantification assay. Data are presented as mean ± SD and analyzed by one-way ANOVA (n = 3 for each sample, *$p < 0.05$).

3.7.2 Osteogenesis potential

Then, we assessed the ability of the nanocomposites to promote osteogenic differentiation, which is a core concern for bone regeneration application. Alkaline phosphatase (ALP) is a critical component of bone matrix vesicles that hydrolyzes the organic phosphate esters and plays a vital role in the initial stages of bone matrix mineralization and is referred to as an early indicator of the osteogenic phenotype [53]. We herein performed the ALP staining to evaluate the osteogenic differentiation of the rMSCs on different material formulations after 0, 3, 7 and 14 days of culture (**Fig. 7**Ai and Aii). The purple ALP staining colonies appeared in all groups after culture for 3 days, and the stained area gradually got larger and denser with the incubation time. By comparison, the ALP positive area was obviously larger on the 50%nHAMA group

than those on other groups on days 3, 7 and 14 (**Fig. 7**Ai). Quantification analysis of ALP activities further confirmed this significant difference that the rMSCs on 50%nHAMA group exhibited the highest ALP activity at 3, 7 and 14 days (**Fig. 7**Aii). Then, Alizarin Red S (ARS) staining was performed to visualize the extracellular matrix mineralization, which was a marker of the late osteogenic efficiency [54]. Both qualitative and quantitative results of ARS assay were consistent with those of ALP assay (**Fig. 7**Bi and Bii); the 50%nHAMA group exhibited significantly higher matrix mineralization compared to other three groups, indicating better osteogenesis potential after implantation. To further elucidate the possible underlying mechanism, the expression level of osteogenic marker genes including Runx2, OCN, Col-1 and ALP were detected by qRT-PCR at 7 days (**Fig. 7**Ci-iv). We found the expression of these genes was drastically upregulated in rMSCs on the 50%nHAMA group, which was in accordance with ALP and ARS assay results outlined.

This phenomenon can be attributed to the synergy effect of the HA supplementation and the increased surface stiffness. The incorporated HA can gradually release Ca^{2+} ions that are a critical second messenger and can induce osteogenic differentiation of the stem cells through the calcium/calmodulin signaling [55]. Here, we measured the Ca^{2+} release from different material formulations (**Fig. S9**). As expected, Ca^{2+} ion released from both 50%nHAMA and 50%nHA were nearly twice to the 30%nHAMA group at all time points. This might explain the 50%nHAMA and 50%nHA groups presented higher osteogenic properties. However, this could not elucidate the significant difference of osteogenic potential between the 50%nHAMA and the 50%nHA groups, since the Ca^{2+} ion released in these two groups was almost the same during the test period. Recently, the profound impacts of matrix stiffness on stem cell responses have been revealed [56]. Particularly, it was reported that the rMSCs tended to differentiate to osteogenic lineages on the stiffer surfaces. Thus, we also examined the expression of mechanosensing-related genes of the rMSCs seeded on different material surfaces (**Fig. 7**Di-iv). Compared with 50%nHA group, the expression levels of the integrin α_2, FAK, ERK1 and ERK2 were significantly upregulated in 50%nHAMA. Combined with the results of mechanical property tests, we speculated that the increased modulus of 50%nHAMA nanocomposite might contribute to the upregulation of integrin α_2 and then induce downstream FAK-ERK pathway activation, promoting the focal adhesion assembly, cytoskeletal organization and ultimate osteogenesis of rMSCs [57]. Altogether, these results suggested that the P_7L_2DMA/50%nHAMA nanocomposite could expedite the osteoinductive and

osteoconductive process as a result of increased Ca^{2+} ion release and the higher surface modulus, making it a fascinating candidate material for bone tissue engineering.

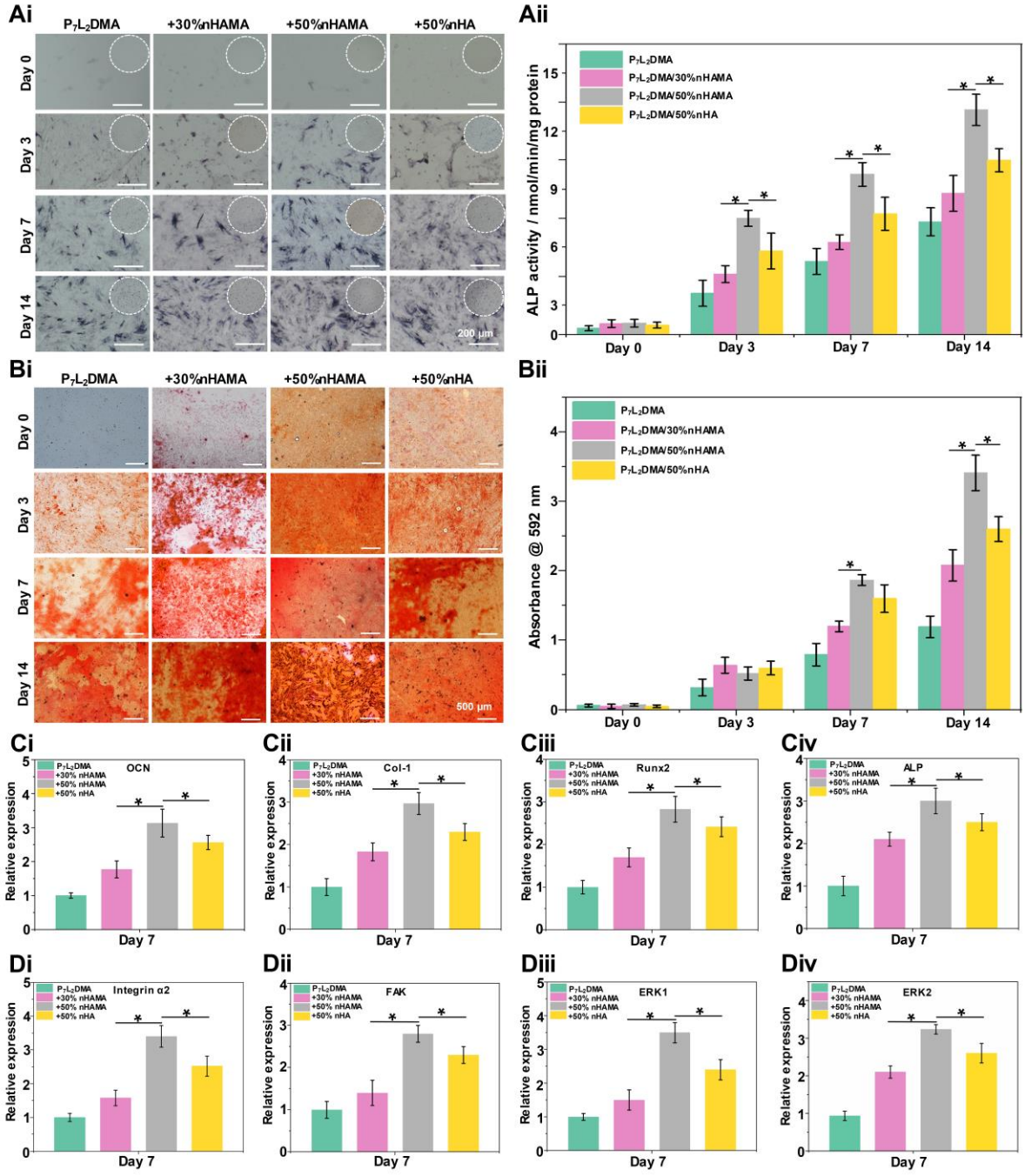

Fig. 7. *In vitro* evaluation of osteogenic differentiation of rMSCs on different material formulations after 0, 3, 7 and 14 days of incubation. (A) ALP assay evaluation: (Ai) representative microscopic images of ALP staining and (Aii) quantitative analysis of ALP activity. (B) ARS assay evaluation: (Bi) representative microscopic images of ARS staining and (Bii) quantitative analysis of matrix mineralization by measuring the absorbance of the

extracted solution at a wavelength of 592 nm with a microplate reader. qRT-PCR analysis of (C) osteogenesis-related gene expressions including (Ci) OCN, (Cii) Col-1, (Ciii) Runx2 and (Civ) ALP, and (D) mechanosensing-related gene expressions including (Di) integrin α_2, (Dii) FAK, (Diii) ERK1 and (Div) ERK2 in rMSCs after culture on different material surfaces for 7 days. Data are presented as mean ± SD and analyzed by one-way ANOVA (n=3 for each group, $^*p < 0.05$).

3.8 *In vivo* biological evaluation

Compared to the solid disc/plug material or the injectable *in situ* cured material, 3D printed scaffolds have showed better bone repair efficacy due to their well-controlled geometry and porous architecture that could match the individual bone defect shape and allow new tissue infiltration [6, 8]. Herein, we adopted 3D printed nanocomposite scaffolds to examine their effects on the *in vivo* bone regeneration. The SEM images confirmed that there was no significant morphology difference among all the scaffolds printed by P_7L_2DMA/50%nHA, P_7L_2DMA/50%nHAMA and P_7L_2DMA/50%nHAMA/BMP-2 composites (Fig. S). The pore size of these scaffolds was around 700 -750 μm. In addition, the reconstructed micro-CT images further demonstrated the interconnected macropore structure inside all scaffolds without significant difference (Fig. S). 6 mm critical-sized defects were first surgically created on the rabbit femoral condyle and then were implanted with P_7L_2DMA/50%nHA and P_7L_2DMA/50%nHAMA scaffolds. Meanwhile, we also printed and implanted a P_7L_2DMA/50%nHAMA scaffold loaded with BMP-2 (P_7L_2DMA/50%nHAMA/BMP-2) to evaluate its performances in *in vivo* BMP-2 delivery and the efficacy in bone repair. An empty hole left untreated on the rabbit femoral condyle was used as the blank control. After implantation for 4 and 8 weeks, Micro-CT analysis was performed to assess how new bone forms within defects (**Fig. 8**A). From the 3D reconstructed images, it could be clearly found that the blank control group presented limited bone regeneration in the defect site even at 8 weeks post-surgery; by contrast, much more new bone formation (red-stained area) was observed in all scaffold groups. Moreover, we found the most part of the scaffolds still remained by 8 weeks. This slow biodegradation behavior *in vivo* was believed highly preferential for an implantable scaffold to realize the balance between the material degradation and new tissue formation [48]. As expected, we also found the 50%nHAMA scaffold group showed better bone healing at both time points than the 50%nHA group, which was in accordance with aforementioned *in vitro* osteogenesis results, demonstrating the increased

mechanical properties could further promote the osteogenesis *in vivo* [58, 59]. In addition, due to the excellent osteoinductive activity of BMP-2, 50%nHAMA/BMP-2 group displayed the most significant new bone formation among the three scaffold groups especially in the short period (4 weeks). Quantitative micro-CT analysis data further confirmed the significantly higher BMD and BV/TV values in the 50%nHAMA group as compared to 50%nHA groups (**Fig. 8**B and C). It also confirmed that 50%nHAMA/BMP-2 group showed the best bone regeneration capacity, with 1.6- and 1.2-fold higher BMD and BV/TV values compared with 50%nHAMA groups. These *in vivo* results demonstrated that the P_7L_2DMA/50%nHAMA scaffolds with or without incorporation of BMP-2 could effectively stimulate the new bone formation of femoral condyle defects during bone healing.

Then, we performed histological examination by Van Gieson's staining to evaluate the osseointegration ability of prepared scaffolds. As shown in **Fig. 8**D, no obvious inflammatory reaction was observed in all groups, confirming the good biocompatibility of our scaffolds *in vivo*. In the first 4 weeks, the new bone formed over the pore edge of the scaffolds in all scaffold groups. Compared with 50%nHA group, there were more cancellous structures in 50% nHAMA and 50%nHAMA/BMP-2 groups. After 8 weeks, new bone tissue grew inside the scaffold pores in all scaffold groups. It was worth noting that these new bones in 50%nHAMA and 50%nHAMA/BMP-2 groups showed much denser Van Gieson's stains than those in the 50%nHA group, and integrated with the surrounding scaffolds more tightly. Quantitative analysis further confirmed that the new bone areas in 50%nHAMA and 50%nHAMA/BMP-2 groups were statistically higher compared to the 50%nHA group, with new bone area of 50%nHAMA/BMP-2 group reaching as high as 80% at week 8 (**Fig. 8**E). These data clearly indicated that our P_7L_2DMA/50%nHAMA scaffolds loading with or without BMP-2 could enhance osseointegration of the scaffolds with the new bone tissue and improve the bone remodeling process, which was consistent with the above micro-CT analysis.

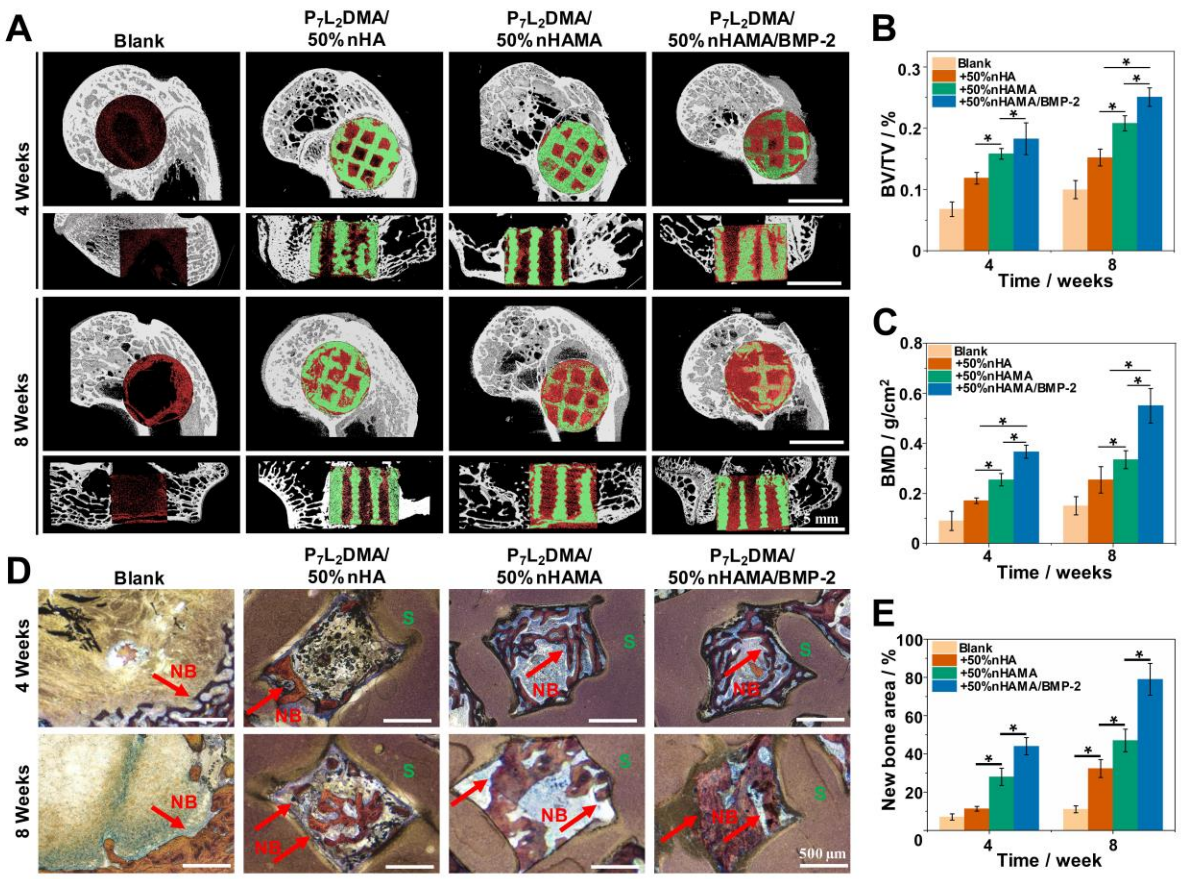

Fig. 8. Micro-CT evaluation and histomorphological observation of the *in vivo* bone regeneration in a rabbit femoral condyle defect model. The femoral condyle defects were implanted with P_7L_2DMA/50%nHA, P_7L_2DMA/50%nHAMA and P_7L_2DMA/50%nHAMA/BMP-2 scaffolds, and the rabbits with no scaffold implantation served as blank control. (A) 3D reconstructed micro-CT images of different groups showing the influences of different samples on the new bone formation after implantation for 4 and 8 weeks. The red color indicated the new bone tissues and green color represents the scaffolds. Quantitative statistic of (B) BV/TV and (C) BMD of the newly formed bone at week 4 and 8. BV/TV: bone volume/total volume; BMD: bone mineral density. (D) Representative images of Van Gieson's staining showing the osseointegration of scaffolds with the new bones. S represented implanted scaffolds and NB indicated new bone tissues. The red-stained areas indicated by the arrows refer to the ossein. (E) Quantitative analysis of the new bone area in the defects. Data are presented as mean ± SD and analyzed by one-way ANOVA (n = 6 for each group, *$p < 0.05$).

4. Conclusion

In summary, we have successfully developed a novel nanocomposite ink consisting of tri-block P_mL_nDMA polymer and nHAMA for bone tissue engineering. Such nanocomposite ink exhibited a remarkable shear-thinning behavior and thixotropic property, and could be fully photocrosslinked within 140 s, desirable for extrusion-based 3D printing. Due to the improved interfacial bonding between nHAMA and P_mL_nDMA through the formation of a covalent co-crosslinked network, the nanocomposite also owned significantly enhanced mechanical properties. Surprisingly, 10- and 9-fold increase in tensile modulus (from 16 to 157 MPa) and compressive modulus (from 43 to 362 MPa) respectively were achieved for the P_7L_2DMA/50%nHAMA composites, compared with the neat P_7L_2DMA, making the printed scaffolds suitable for load-bearing applications. In addition, by simply changing the m and n of the polymer and the content of nHAMA, we found the surface wettability and degradation of the nanocomposite could be readily tuned. Furthermore, this nanocomposite ink enabled not only facile encapsulation of heat-labile biomolecules (e.g., BMP-2) during printing process, but also long-term release of loaded biomolecules for over 60 days. Lastly, both *in vitro* cell studies and *in vivo* osteogenesis assays demonstrated the excellent biocompatibility and osteogenic potential of the printed nanocomposite scaffolds. Taken together, compared with commonly used polymer or composite inks, our P_mL_nDMA/nHAMA nanocomposite ink possessed suitable rheological characteristics, rapid photocrosslinking solidification, adequate mechanical strength and toughness, tunable degradation rate and excellent bioactivity. We thus envisioned our nanocomposite ink an ideal candidate for 3D printing bone grafts.

Declaration of competing interest

The authors declare no competing financial interest.

Data availability

The data used in the present study are available from the corresponding author on reasonable request.

Acknowledgments

This work was supported by the start-up fund (1-ZE7S) and central research fund (G-YBWS) from The Hong Kong Polytechnic University, programme of Jiangsu Health Committee (2018027) and National Natural Science Foundation of China (51675296, 11732105). The

authors would like to thank Mr. Fergus Lam and Chi Hin Hung, Miss. Jane Lam Lok Ching, for their assistance in the project.

References:

[1] H. Ma, C. Jiang, D. Zhai, Y. Luo, Y. Chen, F. Lv, Z. Yi, Y. Deng, J. Wang, J. Chang, A bifunctional biomaterial with photothermal effect for tumor therapy and bone regeneration, Adv. Funct. Mater. 26(8) (2016) 1197-1208. https://doi.org/10.1002/adfm.201504142

[2] R. Agarwal, A.J. García, Biomaterial strategies for engineering implants for enhanced osseointegration and bone repair, Adv. Drug Deliv. Rev. 94 (2015) 53-62. https://doi.org/10.1016/j.addr.2015.03.013

[3] E. García-Gareta, M.J. Coathup, G.W. Blunn, Osteoinduction of bone grafting materials for bone repair and regeneration, Bone 81 (2015) 112-121. https://doi.org/10.1016/j.bone.2015.07.007

[4] S. Bose, M. Roy, A. Bandyopadhyay, Recent advances in bone tissue engineering scaffolds, Trends. Biotechnol. 30(10) (2012) 546-554. https://doi.org/10.1016/j.tibtech.2012.07.005

[5] H. Cui, W. Zhu, B. Holmes, L.G. Zhang, Biologically inspired smart release system based on 3D bioprinted perfused scaffold for vascularized tissue regeneration, Adv. Sci. 3(8) (2016) 1600058. https://doi.org/10.1002/advs.201600058

[6] S. Bose, S. Vahabzadeh, A. Bandyopadhyay, Bone tissue engineering using 3D printing, Mater. Today. 16(12) (2013) 496-504. https://doi.org/10.1016/j.mattod.2013.11.017

[7] L. Ouyang, C.B. Highley, W. Sun, J.A. Burdick, A generalizable strategy for the 3D bioprinting of hydrogels from nonviscous photo‐crosslinkable inks, Adv. Mater. 29(8) (2017) 1604983. https://doi.org/10.1002/adma.201604983

[8] A.E. Jakus, A.L. Rutz, S.W. Jordan, A. Kannan, S.M. Mitchell, C. Yun, K.D. Koube, S.C. Yoo, H.E. Whiteley, C.-P. Richter, Hyperelastic “bone”: A highly versatile, growth factor–free, osteoregenerative, scalable, and surgically friendly biomaterial, Sci. Transl. Med. 8(358) (2016) 358ra127-358ra127. https://doi.org/10.1126/scitranslmed.aaf7704

[9] Y.-H. Huang, A.E. Jakus, S.W. Jordan, Z. Dumanian, K. Parker, L. Zhao, P.K. Patel, R.N. Shah, Three-dimensionally printed hyperelastic bone scaffolds accelerate bone regeneration in critical-size calvarial bone defects, Plast. Reconstr. Surg. 143(5) (2019) 1397-1407. https://doi.org/10.1097/PRS.0000000000005530

[10] S. Knowlton, B. Yenilmez, S. Anand, S. Tasoglu, Photocrosslinking-based bioprinting: Examining crosslinking schemes, Bioprinting 5 (2017) 10-18. https://doi.org/10.1016/j.bprint.2017.03.001

[11] B. Huber, K. Borchers, G.E. Tovar, P.J. Kluger, Methacrylated gelatin and mature adipocytes are promising components for adipose tissue engineering, J. Biomater. Appl. 30(6) (2016) 699-710. https://doi.org/10.1177/0885328215587450

[12] G. Gao, A.F. Schilling, K. Hubbell, T. Yonezawa, D. Truong, Y. Hong, G. Dai, X. Cui, Improved properties of bone and cartilage tissue from 3D inkjet-bioprinted human mesenchymal stem cells by simultaneous deposition and photocrosslinking in PEG-GelMA, Biotechnol. Lett. 37(11) (2015) 2349-2355. https://doi.org/10.1007/s10529-015-1921-2

[13] X. Cui, K. Breitenkamp, M. Finn, M. Lotz, D.D. D'Lima, Direct human cartilage repair using three-dimensional bioprinting technology, Tissue. Eng Part. A. 18(11-12) (2012) 1304-1312. https://doi.org/10.1089/ten.tea.2011.0543
[14] S.B. Kim, Y.J. Kim, T.L. Yoon, S.A. Park, I.H. Cho, E.J. Kim, I.A. Kim, J.-W. Shin, The characteristics of a hydroxyapatite–chitosan–PMMA bone cement, Biomaterials 25(26) (2004) 5715-5723. https://doi.org/10.1016/j.biomaterials.2004.01.022
[15] J. Li, L. Wang, L. Dai, L. Zhong, B. Liu, J. Ren, Y. Xu, Synthesis and characterization of reinforced acrylate photosensitive resin by 2-hydroxyethyl methacrylate-functionalized graphene nanosheets for 3D printing, J. Mater. Sci. 53(3) (2018) 1874-1886. https://doi.org/10.1007/s10853-017-1432-8
[16] C. McBeth, J. Lauer, M. Ottersbach, J. Campbell, A. Sharon, A.F. Sauer-Budge, 3D bioprinting of GelMA scaffolds triggers mineral deposition by primary human osteoblasts, Biofabrication 9(1) (2017) 015009. https://doi.org/10.1088/1758-5090/aa53bd
[17] X. Zhao, Q. Lang, L. Yildirimer, Z.Y. Lin, W. Cui, N. Annabi, K.W. Ng, M.R. Dokmeci, A.M. Ghaemmaghami, A. Khademhosseini, Photocrosslinkable gelatin hydrogel for epidermal tissue engineering, Adv. Healthc. Mater. 5(1) (2016) 108-118. https://doi.org/10.1002/adhm.201500005
[18] O. Jeon, K.H. Bouhadir, J.M. Mansour, E. Alsberg, Photocrosslinked alginate hydrogels with tunable biodegradation rates and mechanical properties, Biomaterials 30(14) (2009) 2724-2734. https://doi.org/10.1016/j.biomaterials.2009.01.034
[19] K.W. Lopez, S.A. Goldstein, M.J. Ciarelli, J.L. Kuhn, M. Brown, L. Feldkamp, The relationship between the structural and orthogonal compressive properties of trabecular bone, J. Biomech. 27(4) (1994) 375-389. https://doi.org/10.1016/0021-9290(94)90014-0
[20] H. Follet, K. Bruyère-Garnier, F. Peyrin, J.-P. Roux, M. Arlot, B. Burt-Pichat, C. Rumelhart, P. Meunier, Relationship between compressive properties of human os calcis cancellous bone and microarchitecture assessed from 2D and 3D synchrotron microtomography, Bone 36(2) (2005) 340-351. https://doi.org/10.1016/j.bone.2004.10.011
[21] X. Pei, L. Ma, B. Zhang, J. Sun, Y. Sun, Y. Fan, Z. Gou, C. Zhou, X. Zhang, Creating hierarchical porosity hydroxyapatite scaffolds with osteoinduction by three-dimensional printing and microwave sintering, Biofabrication 9(4) (2017) 045008. https://doi.org/10.1088/1758-5090/aa90ed
[22] J.A. Driscoll, R. Lubbe, A.E. Jakus, K. Chang, M. Haleem, C. Yun, G. Singh, A.D. Schneider, K.M. Katchko, C. Soriano, 3D-printed ceramic-demineralized bone matrix hyperelastic bone composite scaffolds for spinal fusion, Tissue. Eng. Part A. 26(3-4) (2020) 157-166. https://doi.org/10.1089/ten.TEA.2019.0166
[23] A.K. Gaharwar, N.A. Peppas, A. Khademhosseini, Nanocomposite hydrogels for biomedical applications, Biotechnol. Bioeng. 111(3) (2014) 441-453. https://doi.org/10.1002/bit.25160
[24] X. Zhao, I. Olsen, H. Li, K. Gellynck, P.G. Buxton, J.C. Knowles, V. Salih, A.M. Young, Reactive calcium-phosphate-containing poly (ester-co-ether) methacrylate bone adhesives: Chemical, mechanical and biological considerations, Acta. Biomater. 6(3) (2010) 845-855. https://doi.org/10.1016/j.actbio.2009.09.020

[25] X. Zhao, I. Olsen, J. Pratten, J.C. Knowles, A.M. Young, Reactive calcium-phosphate-containing poly (ester-co-ether) methacrylate bone adhesives: setting, degradation and drug release considerations, J. Mater. Sci. Mater. Med. 22(9) (2011) 1993-2004. https://doi.org/10.1007/s10856-011-4378-4
[26] S.-M. Ho, A.M. Young, Synthesis, polymerisation and degradation of poly (lactide-co-propylene glycol) dimethacrylate adhesives, Eur. Polym. J. 42(8) (2006) 1775-1785. https://doi.org/10.1016/j.eurpolymj.2006.03.018
[27] Q. Liu, J.R. de Wijn, K. de Groot, C.A. van Blitterswijk, Surface modification of nano-apatite by grafting organic polymer, Biomaterials 19(11-12) (1998) 1067-1072. https://doi.org/10.1016/s0142-9612(98)00033-7
[28] Y. Yan, T. Sun, H. Zhang, X. Ji, Y. Sun, X. Zhao, L. Deng, J. Qi, W. Cui, H.A. Santos, Euryale Ferox Seed-Inspired Superlubricated Nanoparticles for Treatment of Osteoarthritis, Adv. Funct. Mater. 29(4) (2019) 1807559. https://doi.org/10.1002/adfm.201807559
[29] H. Chen, T. Sun, Y. Yan, X. Ji, Y. Sun, X. Zhao, J. Qi, W. Cui, L. Deng, H. Zhang, Cartilage matrix-inspired biomimetic superlubricated nanospheres for treatment of osteoarthritis, Biomaterials (2020) 119931. https://doi.org/10.1016/j.biomaterials.2020.119931
[30] E. Colaço, D. Lefèvre, E. Maisonhaute, D. Brouri, C. Guibert, C. Dupont-Gillain, K. El Kirat, S. Demoustier-Champagne, J. Landoulsi, Enzyme-assisted mineralization of calcium phosphate: exploring confinement for the design of highly crystalline nano-objects, Nanoscale 12(18) (2020) 10051-10064. https://doi.org/10.1039/d0nr01638a
[31] C.S. Pfeifer, Z.R. Shelton, R.R. Braga, D. Windmoller, J.C. Machado, J.W. Stansbury, Characterization of dimethacrylate polymeric networks: a study of the crosslinked structure formed by monomers used in dental composites, Eur. Polym. J. 47(2) (2011) 162-170. https://doi.org/10.1016/j.eurpolymj.2010.11.007
[32] J. Skrobot, L. Zair, M. Ostrowski, M. El Fray, New injectable elastomeric biomaterials for hernia repair and their biocompatibility, Biomaterials 75 (2016) 182-192. https://doi.org/10.1016/j.biomaterials.2015.10.037
[33] A. Nandakumar, C. Cruz, A. Mentink, Z.T. Birgani, L. Moroni, C. van Blitterswijk, P. Habibovic, Monolithic and assembled polymer–ceramic composites for bone regeneration, Acta. Biomater. 9(3) (2013) 5708-5717. https://doi.org/10.1016/j.actbio.2012.10.044
[34] S. Kyle, Z.M. Jessop, A. Al-Sabah, I.S. Whitaker, 'Printability'of Candidate Biomaterials for Extrusion Based 3D Printing: State-of-the-Art, Adv. Healthc. Mater. 6(16) (2017) 1700264. https://doi.org/10.1002/adhm.201700264
[35] Y. Wang, W. Cui, X. Zhao, S. Wen, Y. Sun, J. Han, H. Zhang, Bone remodeling-inspired dual delivery electrospun nanofibers for promoting bone regeneration, Nanoscale 11(1) (2019) 60-71. https://doi.org/10.1039/c8nr07329e
[36] K. Wingate, W. Bonani, Y. Tan, S.J. Bryant, W. Tan, Compressive elasticity of three-dimensional nanofiber matrix directs mesenchymal stem cell differentiation to vascular cells with endothelial or smooth muscle cell markers, Acta. Biomater. 8(4) (2012) 1440-1449. https://doi.org/10.1016/j.actbio.2011.12.032
[37] X. Zhao, S. Liu, L. Yildirimer, H. Zhao, R. Ding, H. Wang, W. Cui, D. Weitz, Injectable stem cell-laden photocrosslinkable microspheres fabricated using microfluidics for rapid

generation of osteogenic tissue constructs, Adv. Funct. Mater. 26(17) (2016) 2809-2819. https://doi.org/10.1002/adfm.201504943
[38] X. Zhao, S. Jiang, S. Liu, S. Chen, Z.Y.W. Lin, G. Pan, F. He, F. Li, C. Fan, W. Cui, Optimization of intrinsic and extrinsic tendon healing through controllable water-soluble mitomycin-C release from electrospun fibers by mediating adhesion-related gene expression, Biomaterials 61 (2015) 61-74. https://doi.org/10.1016/j.biomaterials.2015.05.012
[39] H. Gheisari, E. Karamian, M. Abdellahi, A novel hydroxyapatite–hardystonite nanocomposite ceramic, Ceram. Int. 41(4) (2015) 5967-5975. https://doi.org/10.1016/j.ceramint.2015.01.033
[40] T. Xin, Y. Gu, R. Cheng, J. Tang, Z. Sun, W. Cui, L. Chen, Inorganic strengthened hydrogel membrane as regenerative periosteum, ACS Appl. Mater. Interfaces. 9(47) (2017) 41168-41180. https://doi.org/10.1021/acsami.7b13167
[41] S.P. Gentry, J.W. Halloran, Light scattering in absorbing ceramic suspensions: effect on the width and depth of photopolymerized features, J. Eur. Ceram. Soc. 35(6) (2015) 1895-1904. https://doi.org/10.1016/j.jeurceramsoc.2014.12.006
[42] B. Pratap, R.K. Gupta, L. Denis, D. Goswami, Evaluation of polymerization shrinkage and Vickers hardness for restorative dental composites, Mater. Today. 21 (2020) 1563-1565. 10.1016/j.dental.2018.10.003 https://doi.org/10.1016/j.matpr.2019.11.090
[43] M.-J. Kim, R.J.-Y. Kim, J. Ferracane, I.-B. Lee, Thermographic analysis of the effect of composite type, layering method, and curing light on the temperature rise of photo-cured composites in tooth cavities, Dent. Mater. 33(10) (2017) e373-e383. https://doi.org/10.1016/j.dental.2017.07.007
[44] V. Mucci, G. Arenas, R. Duchowicz, W.D. Cook, C. Vallo, Influence of thermal expansion on shrinkage during photopolymerization of dental resins based on bis-GMA/TEGDMA, Dent. Mater. 25(1) (2009) 103-114. https://doi.org/10.1016/j.dental.2008.04.014
[45] C. Liu, Y. Luo, Z. Jia, B. Zhong, S. Li, B. Guo, D. Jia, Enhancement of mechanical properties of poly (vinyl chloride) with polymethyl methacrylate-grafted halloysite nanotube, Express. Polym. Lett. 5(7) (2011) 593-601. https://doi.org/10.3144/expresspolymlett.2011.58
[46] K.J. Rambhia, P.X. Ma, Controlled drug release for tissue engineering, J. Control. Release. 219 (2015) 119-128. 10.1016/j.jconrel.2015.08.049
[47] W.-C. Lin, C. Yao, T.-Y. Huang, S.-J. Cheng, C.-M. Tang, Long-term in vitro degradation behavior and biocompatibility of polycaprolactone/cobalt-substituted hydroxyapatite composite for bone tissue engineering, Dent. Mater. 35(5) (2019) 751-762. https://doi.org/10.1016/j.dental.2019.02.023
[48] K.L. Christman, Biomaterials for tissue repair, Science 363(6425) (2019) 340-341. https://doi.org/10.1126/science.aar2955
[49] C. Zhang, K. Liang, D. Zhou, H. Yang, X. Liu, X. Yin, W. Xu, Y. Zhou, P. Xiao, High-performance photopolymerized poly (vinyl alcohol)/silica nanocomposite hydrogels with enhanced cell adhesion, ACS Appl. Mater. Interfaces. 10(33) (2018) 27692-27700. https://doi.org/10.1021/acsami.8b09026
[50] P. Kerativitayanan, A.K. Gaharwar, Elastomeric and mechanically stiff nanocomposites from poly (glycerol sebacate) and bioactive nanosilicates, Acta. Biomater. 26 (2015) 34-44.

https://doi.org/10.1016/j.actbio.2015.08.025
[51] M.Z. Rong, M.Q. Zhang, Y.X. Zheng, H.M. Zeng, R. Walter, K. Friedrich, Structure–property relationships of irradiation grafted nano-inorganic particle filled polypropylene composites, Polymer 42(1) (2001) 167-183. https://doi.org/10.1016/S0032-3861(00)00325-6
[52] J. Malda, J. Visser, F.P. Melchels, T. Jüngst, W.E. Hennink, W.J. Dhert, J. Groll, D.W. Hutmacher, 25th anniversary article: engineering hydrogels for biofabrication, Adv. Mater. 25(36) (2013) 5011-5028. https://doi.org/10.1002/adma.201302042
[53] Y. Mikami, H. Tsuda, Y. Akiyama, M. Honda, N. Shimizu, N. Suzuki, K. Komiyama, Alkaline phosphatase determines polyphosphate-induced mineralization in a cell-type independent manner, J. Bone. Miner. Metab. 34(6) (2016) 627-637. https://doi.org/10.1007/s00774-015-0719-6
[54] W.-T. Su, W.-L. Chiou, H.-H. Yu, T.-Y. Huang, Differentiation potential of SHEDs using biomimetic periosteum containing dexamethasone, Mater. Sci. Eng. C. 58 (2016) 1036-1045. https://doi.org/10.1016/j.msec.2015.09.077
[55] Y.C. Chai, A. Carlier, J. Bolander, S.J. Roberts, L. Geris, J. Schrooten, H. Van Oosterwyck, F.P. Luyten, Current views on calcium phosphate osteogenicity and the translation into effective bone regeneration strategies, Acta. Biomater. 8(11) (2012) 3876-3887. https://doi.org/10.1016/j.actbio.2012.07.002
[56] H. Lv, L. Li, M. Sun, Y. Zhang, L. Chen, Y. Rong, Y. Li, Mechanism of regulation of stem cell differentiation by matrix stiffness, Stem. Cell. Res. Ther. 6(1) (2015) 103. https://doi.org/10.1186/s13287-015-0083-4
[57] Y.R.V. Shih, K.F. Tseng, H.Y. Lai, C.H. Lin, O.K. Lee, Matrix stiffness regulation of integrin - mediated mechanotransduction during osteogenic differentiation of human mesenchymal stem cells, J. Bone. Miner. Res. 26(4) (2011) 730-738. https://doi.org/10.1002/jbmr.278
[58] G. Chen, C. Dong, L. Yang, Y. Lv, 3D scaffolds with different stiffness but the same microstructure for bone tissue engineering, ACS Appl. Mater. Interfaces. 7(29) (2015) 15790-15802. https://doi.org/10.1021/acsami.5b02662
[59] A. Cipitria, K. Boettcher, S. Schoenhals, D.S. Garske, K. Schmidt-Bleek, A. Ellinghaus, A. Dienelt, A. Peters, M. Mehta, C.M. Madl, In-situ tissue regeneration through SDF-1α driven cell recruitment and stiffness-mediated bone regeneration in a critical-sized segmental femoral defect, Acta. Biomater. 60 (2017) 50-63. https://doi.org/10.1016/j.actbio.2017.07.032